Fully implicit methodology for the dynamics of biomembranes and capillary interfaces by combining the level set and Newton methods

CrossMark

Aymen Laadhari [a],[*], Pierre Saramito [b], Chaouqi Misbah [c], Gábor Székely [a]

[a] Computer Vision Laboratory, Institut für Bildverarbeitung, Department of Information Technology and Electrical Engineering, Swiss Federal Institute of Technology Zürich (Eidgenössische Technische Hochschule Zürich, ETH-Zentrum), CH-8092 Zürich, Switzerland
[b] Laboratoire Jean Kuntzmann (LJK), CNRS and Université Grenoble Alpes, F-38000 Grenoble, France
[c] Laboratoire interdisciplinaire de physique (LIPHY), CNRS and Université Grenoble Alpes, F-38000 Grenoble, France

ARTICLE INFO

ABSTRACT

This framework is concerned with the numerical modeling of the dynamics of individual biomembranes and capillary interfaces in a surrounding Newtonian fluid. A level set approach helps to follow the interface motion. Our method features the use of high order fully implicit time integration schemes that enable to overcome stability issues related to the explicit discretization of the highly non-linear bending force or capillary force. At each time step, the tangent systems are derived and the resulting nonlinear problems are solved by a Newton–Raphson method. Based on the signed distance assumption, several inexact Newton strategies are employed to solve the capillary and vesicle problems and guarantee the second-order convergence behavior. We address in detail the main features of the proposed method, and we report several experiments in the two-dimensional case with the aim of illustrating its accuracy and efficiency. Comparative investigations with respect to the fully explicit scheme depict the stabilizing effect of the new method, which allows to use significantly larger time step sizes.

© 2017 Elsevier Inc. All rights reserved.

1. Introduction

In this paper, we aim at presenting a new methodology to solve numerically the time dependent coupled Navier–Stokes and level set equations. This new approach avoids the usual stability conditions and time step restrictions that hold when fully explicit schemes are considered. The previous coupled equations are used for the modeling of two applications: the dynamics of interfacial flows with surface tension and the dynamics of vesicles mimicking red blood cells, referred to as RBCs, in a Newtonian flow. Let us briefly review these applications.

Surface tension is involved in liquid surface as an elastic skin, because the fluid molecules near the surface develop molecular forces of attraction. At the continuous level, the resulting surface force acts locally on the fluid at the interface along the normal direction except if it depends on the position along the surface [1,2]. The fluid interface motion induced by the surface tension plays a fundamental role in many natural and industrial phenomena. Without exhaustivity, let us

---

* Corresponding author.
E-mail addresses: laadhari@vision.ee.ethz.ch (A. Laadhari), Pierre.Saramito@imag.fr (P. Saramito), chaouqi.misbah@univ-grenoble-alpes.fr (C. Misbah), szekely@vision.ee.ethz.ch (G. Székely).

mention capillarity, low-gravity fluid flow, hydrodynamic stability, surfactant behavior, cavitation, droplet dynamics in clouds and in fuel sprays used in internal combustion engines. Detailed analyses of these phenomena typically involve the use of numerical computations. Advancing the computational understanding of these industrial processes can certainly be of great potential in the improvement of the underlying technologies. A growing literature has been devoted to the computational modeling of the dynamics of interfacial flows with surface tension. Several methodologies have been developed and we refer the interested readers to review papers, for example, by Rider et al. [3], Scardovelli et al. [4], Sethian et al. [5], Gross et al. [6] or Anna [7]. Most of these methods are also used for vesicles and RBCs problems, but with several additional difficulties.

Red blood cells represent the major cellular component of blood, occupying almost 44% of its total volume. Mature human RBCs have a characteristic dimension of $\approx 8 \times 2$ μm and are made of a phospholipid bilayer ($\approx 4/5$ nm of thickness) connected to an inner spectin cytoskeleton network ($\approx 60/80$ nm) and an outer glycocalyx (carbohydrate-rich) layer. The main tasks of RBCs consist of delivering oxygen (hemoglobin is the main oxygen carrier) and capturing carbone dioxyde through blood circulation. Giant unilamellar vesicles (≈ 10 μm of diameter) are artificial liquid drops which are biomimetics. They are used in vitro and in silico to study the mechanical behavior of RBCs. The study of the deformations of RBCs is a tremendously challenging topic in theoretical and computational modeling, attracting a growing interest over the past decade [8,9]. Researches have covered the fields of experimental biology [10], theoretical biology [11], physics [12,8,13] and applied mathematics [14,15].

To model the mechanical properties of the RBC's membrane, Canham [16], Helfrich [17,18] and Evans [19] introduced independently a model in the early 1970s, in which the main mode of the deformation is bending, and the cost in the bending energy is driven by the curvatures of the membrane (quadratic). A bending force highly nonlinear with respect to the cell's shape drives consequently the deformations of RBCs [20]. Several computational methodologies have been developed to study the static equilibrium [21–24] and the hydrodynamics [25,26,15] of RBCs. They can be roughly sorted according to the strategy used to address the fluid and membrane coupling: the phase field approach [27,28], the level set approach in finite difference [29] or finite element context [30–33], the boundary integral method [34,35], the immersed boundary method [36,37], the interfacial spectral boundary element method [38], the parametric finite element method [15, 39,40] and the lattice Boltzmann method [41].

Regarding the interaction with the surrounding fluid dynamics, fully explicit decoupling approaches of the surface tension or bending force are usually considered, in particular when using the classical finite element method (see e.g. [26,32]). The major drawbacks of such decoupling strategies is the numerical issues related to the stability of the solver, which become more problematic especially when large interface deformations happen. Indeed, a severe stability conditions results in the restriction of the time step size which depends on both the mesh size and the coefficient of surface tension or bending rigidity. To the knowledge of the authors, few coupling strategies which are implicit or semi-implicit in time have been introduced in the existing literature in finite element and finite volume frameworks for the surface tension problem (see e.g. [42–44]). For the vesicle problem, only semi-implicit strategies using the parametric FEM have been developed [15, 39,40]. Recently, Laadhari et al. [31] proposed an implicit and sequential approach based on a fixed point algorithm for solving at each time step the nonlinear coupling between equations in the vesicle problem. However, the convergence of this strategy is sometimes very slow due to the high nonlinearity of the operators.

In the present work we describe a fully implicit and monolithic approach, based on the Newton method [45], to solve the highly nonlinear coupled system modeling the dynamics of vesicles in flow. The appealing feature of quadratic convergence of the Newton method is obtained, as depicted in the numerical examples. To address the singularity of the linear system corresponding to the vesicle problem and maintain a reasonable computational cost compared to the classical explicit approach, we introduce a banded level set technique that allows to assemble the integrals over the membrane only in a banded strip near the membrane. Accordingly, the Lagrange multiplier enforcing the local inextensibility characterizing biomembranes [31] is only defined in the latter strip domain. A modified redistancing problem is solved on a rolling basis, while avoiding the singular values of the outward normal vector near the skeleton [24] of the level set function. In virtue of the signed distance property, we introduce inexact Newton strategies for the vesicle and surface tension problems which ensures, in addition to the parallel implementation, additional computational savings. Finally, we test the accuracy of the inexact Newton method in both cases of a rising bubble under capillary forces and single vesicle under bending forces.

We have arranged the remainder of this paper as follows. Section 2 presents the mathematical formulation of the vesicle and surface tension problems. It starts with some notations and concepts used throughout the paper. A short description of the physical problems and the Eulerian formulations in a level set framework are provided. The nonlinear coupled problems and the variational formulations are subsequently presented. Section 3 starts with the second order time discretization of the problems. It then describes the exact Newton and quasi-Newton strategies for both surface tension and vesicle problems. The space discretization, in a finite element framework, is then elaborated. A set of numerical examples showing the main features and the accuracy of the methodology are described in section 4. We close with some remarks on the model limitations and current extensions in Section 5. Details on the linearization procedure, the exact Jacobian matrix for the vesicle problem and the mass lumping technique are provided in the appendices.
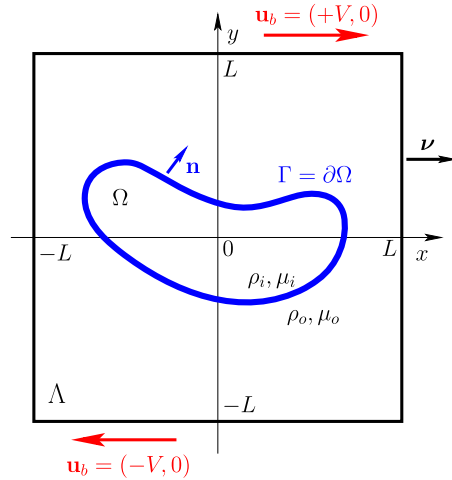
Fig. 1. A representation of the interface or membrane embedded in a larger computational domain Λ. In the present applications, the region Ω contains a bubble or a vesicle.

2. Problem statement

Let $T > 0$ represent the final time of the experiment. At any time $t \in (0, T)$, the region occupied by a drop or a vesicle is denoted by $\Omega(t) \subset \mathbb{R}^2$. This region is embedded in a surrounding fluid and let Λ denote the whole domain of computation, see Fig. 1. In applications, a drop could be a gas or a liquid in another surrounding liquid, or a vesicle or RBC in plasma. We assume that the boundary $\Gamma(t) = \partial\Omega(t)$ is Lipschitz continuous. We also assume that the whole domain is sufficiently large such that $\Gamma(t) \cap \partial\Lambda = \emptyset$, for all $t \in (0, T)$. Let $\boldsymbol{n}$ and $\boldsymbol{\nu}$ denote the unit outward normal vector on the interface $\Gamma(t)$ and on the boundary of the whole domain $\partial\Lambda$, respectively. Let us first introduce some surface operators needed afterwards. The surface gradient operator $\boldsymbol{\nabla}_s$, the surface divergence operator div_s and the Laplace–Beltrami operator Δ_s are defined, for any scalar function $\varkappa$ and vector valued function $\boldsymbol{v}$, by

$$\boldsymbol{\nabla}_s\varkappa = (\mathbf{Id} - \boldsymbol{n} \otimes \boldsymbol{n})\,\boldsymbol{\nabla}\varkappa, \qquad \text{div}_s\,\boldsymbol{v} = \text{tr}(\boldsymbol{\nabla}_s\boldsymbol{v}) = (\mathbf{Id} - \boldsymbol{n} \otimes \boldsymbol{n}) : \boldsymbol{\nabla}\boldsymbol{v} \qquad \text{and} \qquad \Delta_s\varkappa = \text{div}_s\,(\boldsymbol{\nabla}_s\varkappa)\,.$$

Here, $\mathbf{Id}$ denotes the identity tensor, while the symbols "$\otimes$" and "$:$" are the tensorial product and the two times contracted product between tensors, respectively. The mean and Gauss curvatures are denoted H and K, respectively, and are defined as the sum and the product of the principle curvatures on $\Gamma(t)$. Notice that the mean curvature expresses in terms of the normal vector as $H = \text{div}_s\,\boldsymbol{n}$. We thereafter present the energy and forces that drive the motion of $\Omega(t)$ and the interface $\Gamma(t)$.

From now, the explicit dependence of Ω and Γ from t will be understood.

2.1. Surface tension energy and capillary force

Modeling flows with two immiscible fluids with surface tension effects involves the interface energy:

$$\mathcal{J}(\Omega) = \lambda \int_{\Gamma} \mathrm{d}\boldsymbol{s},$$

where λ represents the surface tension coefficient which is assumed to be constant. The immiscible two-fluid dynamics is subject to a specific constraint. Indeed, both fluids are assumed incompressible and the volume of each fluid is locally conserved. Let $\boldsymbol{u}$ denote the fluid velocity field. The constrained space of admissible velocities writes:

$$\left\{ \boldsymbol{u} : \quad \text{div}\,\boldsymbol{u} = 0 \text{ in } \Lambda \right\}.$$

In other words, at equilibrium, the system of two immiscible and incompressible fluids minimizes the perimeter of its interface while conserving the mass of each of the two fluids. The surface tension force on the interface expresses as:

$$\boldsymbol{F}_{\Gamma} = \lambda H \boldsymbol{n} \quad \text{on } (0, T) \times \Gamma. \tag{2.1}$$

2.2. Membrane bending energy and bending force

Following the Canham–Helfrich–Evans model, the cell movement is dictated by the interplay between the hydrodynamic forces and the membrane force characterized by the scalar stored-energy functions:

$$\mathcal{J}(\Omega) = \frac{k_b}{2} \int_\Gamma \left(H(\Omega) - \kappa_0 \right)^2 \mathrm{d}\boldsymbol{s} + k_g \int_\Gamma K(\Omega)\, \mathrm{d}\boldsymbol{s}, \tag{2.2}$$

where k_b represents the bending rigidity modulus typically $\approx 10^{-20}/10^{-19}$ kg m^2 s^{-2} for phospholipidic membranes [40] and k_g is the Gaussian curvature modulus. The energy is a variant of the Willmore energy [46,47]. The energy term weighted by k_g is invariant within a fixed topology class, by the virtue of the Gauss–Bonnet theorem [23], and is thereafter disregarded. We also disregard the spontaneous curvature κ_0 which describes the asymmetry of the membrane's curvature at rest, resulting from different chemical environment on both sides of the bilayer Γ.

The lipid bilayer mechanics is subject to specific constraints. First, the impermeability of the membrane results in an osmotic pressure, for which the intra- and extra-compartmental fluids are assumed incompressible. In addition, the local inextensibility characterizes biological membranes, and we assume that no matter exchange happens between the intracellular and the extracellular compartments. The local incompressibility corresponds to a zero surface divergence, and it results in preserving the membrane area thanks to the Reynolds lemma [31]. Analogously to the capillary problem, let λ stand for the membrane tension in the vesicle problem; λ acquires the meaning of a Lagrange multiplier corresponding to the membrane inextensibility constraint. We emphasize that, unlike the capillary problem, the membrane tension λ is now spatially varying and represents an unknown of the vesicle problem. Therefore, the membrane tension field will be computed as a part of the problem. To summarize, the constrained space of admissible velocities writes:

$$\left\{ \boldsymbol{u} : \quad \mathrm{div}\, \boldsymbol{u} = 0 \text{ in } \Lambda \quad \text{and} \quad \mathrm{div}_s \boldsymbol{u} = 0 \text{ on } \Gamma \right\}.$$

We refer to our previous derivations using a shape differentiation approach in [20], where the bending force expresses in the two-dimensional case as:

$$\boldsymbol{F}_\Gamma = \frac{k_b}{2} \left(2\Delta_s H + H^3 \right) \boldsymbol{n} \quad \text{on } (0, T) \times \Gamma. \tag{2.3}$$

2.3. Level set formulation

The motion of the interface Γ is followed in an Eulerian framework as the zero level set of a signed distance function φ. For any $t \in (0, T)$, the motion of the interface is given by:

$$\frac{\partial \varphi}{\partial t} + \boldsymbol{u} \cdot \nabla \varphi = 0 \quad \text{in } (0, T) \times \Lambda. \tag{2.4}$$

The transport equation is initialized with a distance function φ_0 associated to the initial interface $\Gamma(0)$. All geometrical quantities such as $\boldsymbol{n}$, H, K and $\boldsymbol{F}_\Gamma$ are naturally encoded in terms of φ and are consequently extended to the entire Λ.

To avoid using meshes that fit the interface Γ, a regularization approach is commonly used. Let ε represent a regularization parameter proportional to the mesh size, referred to as h. The sharp Heaviside function $\mathcal{H}$ and the Dirac measure δ_Γ are regularized within a banded strip of width 2ε such that:

$$\mathcal{H}_\varepsilon(\varphi) = \begin{cases} 0, & \text{if } \varphi < -\varepsilon \\ \dfrac{1}{2}\left(1 + \dfrac{\varphi}{\varepsilon} + \dfrac{\sin\left(\dfrac{\pi\varphi}{\varepsilon}\right)}{\pi} \right), & \text{if } |\varphi| \leqslant \varepsilon \\ 1, & \text{otherwise} \end{cases} \quad \text{and} \quad \delta_\varepsilon(\varphi) = \begin{cases} \dfrac{1}{2\varepsilon}\left(1 + \cos\left(\dfrac{\pi\varphi}{\varepsilon}\right) \right), & \text{if } |\varphi| \leqslant \varepsilon \\ 0, & \text{otherwise.} \end{cases}$$

In addition, we introduce a regularized sign function that provides the sign of the level set function. It is given by $S_\varepsilon(\varphi) = 2\mathcal{H}_\varepsilon(\varphi) - 1$.

A classical difficulty is that the signed distance property is lost during the advection of the level set, resulting in problematic scenarios where the gradient becomes too large or too small near Γ, worsening consequently the accurate computations over Γ. A "redistancing approach" is commonly solved to reestablish the signed distance property [48,49], while keeping invariant the iso-surface $\varphi = 0$. However, it is well-known that the classical approach [48,49] results in significant displacement of the zero level set and induces substantial errors during the redistancing process. To circumvent this problem, several approaches have been proposed in the published literature and enable to reduce the unphysical shift of the iso-surface $\varphi = 0$ during the redistancing process. Some strategies rely on increased mesh resolution or adaptive refinement near $\varphi = 0$ [50–52]. Some other approaches are based on the modification of the classical formulation [53], or introduce an explicit forcing term that allows to fix the zero level set during the redistancing [54–56,31,24]. In the present work, we use the approach described in [31].

Another classical difficulty related to the redistancing consists in the existence of a singular zone, referred to as the skeleton, in which the normal vector becomes discontinuous, see [24] for a concrete description. Solving the redistancing problem may worsen the solution near the skeleton and induces wrong sets where φ becomes equal to zero near the

skeleton. To address this problem, we introduce an extra diffusion term acting only in the vicinity of the skeleton and calibrated by a small parameter α. That enables to regularize the level set function near the skeleton without any changes in the approach introduced in [24]. Let X_ε be a regularized characteristic function of the domain $\{\boldsymbol{x} \in \Lambda : \varphi(\boldsymbol{x}) \leqslant -2\varepsilon\}$.

Let τ be a pseudo-time variable introduced at any time $t \in (0, T)$. We shall solve the following problem until the convergence is achieved:

$$\frac{\partial \phi}{\partial \tau}(\tau, \cdot; t) + S_\varepsilon(\varphi(t, \cdot))\Big(|\nabla\phi(\tau, \cdot; t)| - 1\Big) - \alpha X_\varepsilon \Delta\phi(\tau, \cdot; t) + \xi(\tau, \cdot; t) = 0 \qquad \text{in } (0, +\infty) \times \Lambda \qquad (2.5)$$

$$\phi(0, \cdot; t) = \varphi(t, \cdot) \qquad \qquad \text{in } \Lambda.$$

where $S_\varepsilon(\varphi)$ enables to impose a zero-displacement for the zero level set Γ, and the Lagrange multiplier $\xi(\tau, \cdot; t)$ acts as an explicit forcing term that locally enforces a constant volume of any arbitrary patch in Λ, see [31] for a detailed description. When the convergence is reached, the level set $\varphi(t, \cdot)$ is updated by the solution $\phi(\infty, \cdot; t)$. At the numerical level, we use a first order combined characteristic and finite difference discretization method to approximate the material derivative in (2.5), see [57].

2.4. Statement of the nonlinear coupled problem

We assume constant fluid density $\rho_{i/o}$ and viscosity $\mu_{i/o}$ in both sides of the membrane Γ, where the subscripts "i" and "o" stand for the intracellular and extracellular domains, respectively. Let X_Ω represent the characteristic function of Ω. The global density and viscosity functions are given by:

$$\rho(\varphi) = \rho_i X_\Omega + \rho_o X_{\Lambda \setminus \Omega} \qquad \text{and} \qquad \mu(\varphi) = \mu_i X_\Omega + \mu_o X_{\Lambda \setminus \Omega}.$$

Let $\boldsymbol{\sigma}(\boldsymbol{u}, p, \varphi) = 2\mu(\varphi)\mathbf{D}(\boldsymbol{u}) - p\boldsymbol{I}$ and $\mathbf{D}(\boldsymbol{u}) = (\nabla\boldsymbol{u} + \nabla\boldsymbol{u}^T)/2$ be the fluid Cauchy stress and the strain tensors, respectively. We introduce two complementary subsets Σ_D and Σ_N of the boundary $\partial\Lambda$ (to be subsequently specified for each example) on which either essential or natural boundary conditions are assigned, respectively. Let $\boldsymbol{u}_b$ represent the shear velocity on Σ_D, while φ_b represents the level set on the upstream boundary $\Sigma_- = \Big\{\boldsymbol{x} \in \partial\Lambda : \boldsymbol{u} \cdot \boldsymbol{v}(\boldsymbol{x}) < 0\Big\}$. We introduce the functional spaces of admissible velocities, pressures, membrane tension and level set:

$$\mathbb{V}(\boldsymbol{u}_b) = \left\{\boldsymbol{v} \in \left(H^1(\Lambda)\right)^2 : \boldsymbol{v} = \boldsymbol{u}_b \text{ on } \Sigma_D\right\}, \qquad \mathbb{Q} = \left\{q \in L^2(\Lambda) : \int_\Omega q \, d\boldsymbol{x} = 0\right\}, \qquad \mathbb{W} = \left\{\xi \in H^{-1/2}(\Gamma)\right\},$$

$$\mathbb{X} = \left\{\psi \in W^{1,\infty}(\Lambda) \cap H^1(\Lambda)\right\} \qquad \text{and} \qquad \mathbb{X}(\varphi_b) = \mathbb{X} \cap \left\{\psi \in L^\infty(\Lambda) : \psi = \varphi_b \text{ on } \Sigma_-\right\}.$$

Thereafter, we first state the vesicle problem, while the surface tension problem is subsequently described.

Let $[\boldsymbol{u}]_-^+ = \boldsymbol{u}_+ - \boldsymbol{u}_-$ and $[\boldsymbol{\sigma}\boldsymbol{n}]_-^+ = \boldsymbol{\sigma}_+\boldsymbol{n} - \boldsymbol{\sigma}_-\boldsymbol{n}$ denote the jumps in velocity and normal stress across the interface, respectively. The jump in the normal stress across Γ comes from the balance with the membrane strengths [31] and it describes the interactions between the vesicle and its surrounding fluid. We assume that $[\boldsymbol{u}]_-^+ = \boldsymbol{0}$, while the stress discontinuity is calibrated according to the membrane tension and the bending rigidity:

$$\left[\boldsymbol{\sigma}\boldsymbol{n}\right]_-^+ = \nabla_s\lambda - \lambda H\boldsymbol{n} + k_b\left(\Delta_s H + \frac{H^3}{2}\right)\boldsymbol{n} \qquad \text{on } (0, T) \times \Gamma.$$

To present the dimensionless problem, some dimensionless quantities of hemodynamical relevance are first introduced. The Reynolds number $\mathrm{Re} = \rho U D \mu_o^{-1}$ expresses the ratio between the inertial forces and the viscous effects, in which U is the maximum instantaneous velocity U on Σ_D and D is the diameter of a circle having the same perimeter as the cell. The capillary number $\mathrm{Ca} = \mu_o D^2 U k_b^{-1}$ compares the strength of the imposed flow to the bending resistance of the membrane. The confinement $\gamma = D/D_v$ compares the cell size to the width D_v of the domain. The viscosity ratio $\mu^\star = \mu_i/\mu_o$ expresses the intracellular viscosity with respect to the extracellular viscosity, while we assume almost similar values of the intra- and extracellular densities yielding $\rho^\star = \rho_i/\rho_o \approx 1$. Finally, the cell deflation is given in the two-dimensional case by the dimensionless reduced area $\chi = 4\pi|\Omega|/|\Gamma|^2 \in [0, 1]$ which expresses the ratio between the vesicle's area and the area of a circle having the same perimeter. In what follows, all the quantities are dimensionless, while we keep using the same previous notation for the new dimensionless variables for ease of exposition. By testing with suitable test functions and integrating the momentum equation on both Ω and $\Lambda\setminus\overline{\Omega}$ separately, the variational formulation of the dimensionless problem reads:

$\mathscr{P}$: *find* $\boldsymbol{u} \in \mathcal{C}^0\left((0, T), L^2(\Lambda)^2\right) \cap L^2\left((0, T), \mathbb{V}(\boldsymbol{u}_b)\right)$, $p \in L^2\left((0, T), \mathbb{Q}\right)$, $\lambda \in L^2\left((0, T), \mathbb{W}\right)$ *and* $\varphi \in \mathcal{C}^0\left((0, T), L^2(\Lambda)^2\right) \cap L^2\left((0, T), \mathbb{X}(\varphi_b)\right)$ *such that*

$$\text{Re} \int_\Lambda \rho(\varphi) \left(\frac{\partial \boldsymbol{u}}{dt} + \boldsymbol{u} \cdot \nabla \boldsymbol{u} \right) \cdot \boldsymbol{v} + \int_\Lambda 2\mu(\varphi) \, \mathbf{D}(\boldsymbol{u}) : \mathbf{D}(\boldsymbol{v}) - \int_\Lambda p \, \text{div} \, \boldsymbol{v} - \int_\Gamma \lambda \, \text{div}_s \, \boldsymbol{v}$$

$$- \frac{1}{2\text{Ca}} \int_\Gamma \left(2\Delta_s H + H^3 \right) \boldsymbol{n} \cdot \boldsymbol{v} = \int_{\Sigma_N} \boldsymbol{\sigma} \boldsymbol{v} \cdot \boldsymbol{v}, \qquad \forall \boldsymbol{v} \in \mathbb{V}(0), \tag{2.6}$$

$$\int_\Lambda q \, \text{div} \, \boldsymbol{u} = 0, \qquad \forall q \in \mathbb{Q}, \tag{2.7}$$

$$\int_\Gamma \xi \, \text{div}_s \, \boldsymbol{u} = 0, \qquad \forall \xi \in \mathbb{W}, \tag{2.8}$$

$$\int_\Lambda \frac{\partial \varphi}{\partial t} \psi + \int_\Lambda (\boldsymbol{u} \cdot \nabla \varphi) \, \psi = 0, \qquad \forall \psi \in \mathbb{X}(0). \tag{2.9}$$

Regarding the surface tension problem, the continuity of the velocity across the interface writes $[\boldsymbol{u}]_-^+ = \boldsymbol{0}$, while the stress discontinuity is calibrated according to the surface tension such that

$$\left[\boldsymbol{\sigma} \boldsymbol{n} \right]_-^+ = \lambda \, H \boldsymbol{n} \qquad \text{on } (0, T) \times \Gamma.$$

In addition, we consider the external gravitational force given by $\boldsymbol{g} \approx (0, -0.98)^T$. From now, the dimensionless counterpart is rather denoted $\boldsymbol{g} = (0, -1)^T$. The dimensionless Reynolds number reads $\text{Re} = \rho_o U_g D / \mu_o$, where ρ_o, μ_o, D and $U_g = \sqrt{D|\boldsymbol{g}|}$ design the density and the viscosity of the surrounding heavier fluid, the diameter of the bubble at the initial position and the gravitational velocity. The dimensionless Eötvös number $\text{Eo} = \rho_o U_g^2 D / \lambda$ compares the gravitational forces to the surface tension effects, while the dimensionless capillary number is given by the ratio $\text{Ca} = \text{Eo}/\text{Re}$. The weak formulation of the non-dimensionalized momentum equation reads:

$$\text{Re} \int_\Lambda \rho(\varphi) \left(\frac{\partial \boldsymbol{u}}{\partial t} + \boldsymbol{u}.\nabla \boldsymbol{u} \right) \cdot \boldsymbol{v} + \int_\Lambda 2\mu(\varphi) \mathbf{D}(\boldsymbol{u}) : \mathbf{D}(\boldsymbol{v}) - \int_\Lambda p \, \text{div} \, \boldsymbol{v} = \text{Re} \int_\Lambda \rho(\varphi) \boldsymbol{g} \cdot \boldsymbol{v} + \frac{1}{\text{Ca}} \int_\Gamma H \boldsymbol{n} \cdot \boldsymbol{v}. \tag{2.10}$$

The surface tension problem is given by the coupled system: the momentum equation (2.10), the continuity equation (2.7) and the level set equation (2.9).

In a purely Eulerian framework, all integrals over the moving membrane Γ are transformed into integrals over the entire domain Λ. For any given function $\eta(\cdot)$ defined on Γ, an extension $\tilde{\eta}(\cdot)$ to Λ is required to approximate the surface integrals in such a way that:

$$\int_\Gamma \eta(\boldsymbol{x}) \, d\boldsymbol{s} = \int_\Lambda |\nabla \varphi| \, \delta_\Gamma \, \tilde{\eta}(\boldsymbol{x}) \, d\boldsymbol{x} \approx \int_\Lambda |\nabla \varphi| \, \delta_\varepsilon(\varphi) \, \tilde{\eta}(\boldsymbol{x}) \, d\boldsymbol{x}. \tag{2.11}$$

In addition, the regularized viscosity and density functions are given by:

$$\mu_\varepsilon(\varphi) = \mu^\star + (1 - \mu^\star) \mathscr{H}_\varepsilon(\varphi) \qquad \text{and} \qquad \rho_\varepsilon(\varphi) = \rho^\star + (1 - \rho^\star) \mathscr{H}_\varepsilon(\varphi).$$

3. Numerical methods

3.1. Second order time discretization

Let us divide $[0, T]$ into N subintervals $[t_n, t_{n+1})$, $n = 0, \ldots, N - 1$ of constant step size Δt. For any $n \geqslant 1$, the unknowns $\boldsymbol{u}^n$, p^n, λ^n and φ^n at time step n are computed by induction, using values at previous time steps. The backward differentiation scheme of second order, referred to as BDF2, is used for the momentum (2.6) and the level set (2.9) equations. The scheme is bootstrapped by the initial conditions $\boldsymbol{u}^{-1} = \boldsymbol{u}^0 = \boldsymbol{u}_0$ and $\varphi^{-1} = \varphi^0 = \varphi_0$, where $\boldsymbol{u}^{-1}$ and φ^{-1} only stand for convenient notations. The time derivative terms of the velocity $\boldsymbol{u}$ and the level set φ are approximated by:

$$\frac{\partial \boldsymbol{u}}{\partial t} \approx \frac{3\boldsymbol{u}^n - 4\boldsymbol{u}^{n-1} + \boldsymbol{u}^{n-2}}{2\Delta t} \qquad \text{and} \qquad \frac{\partial \varphi}{\partial t} \approx \frac{3\varphi^n - 4\varphi^{n-1} + \varphi^{n-2}}{2\Delta t}.$$

The semi-discrete approximation in time of $\mathscr{P}$ reads:

$(\mathscr{P}^n)$ *find* $\boldsymbol{u}^n$, p^n, λ^n *and* φ^n *such that:*

$$\text{Re} \int_\Lambda \rho(\varphi^n) \left(\frac{3\boldsymbol{u}^n - 4\boldsymbol{u}^{n-1} + \boldsymbol{u}^{n-2}}{2\Delta t} + \boldsymbol{u}^n \cdot \nabla \boldsymbol{u}^n \right) \cdot \boldsymbol{v} + \int_\Lambda 2\mu(\varphi^n) \, \mathbf{D}\left(\boldsymbol{u}^n \right) : \mathbf{D}(\boldsymbol{v}) - \int_\Lambda p^n \, \text{div} \, \boldsymbol{v}$$

$$-\int_{\Gamma^n} \lambda^n \, \mathrm{div}_s^n \, \boldsymbol{v} - \frac{1}{2\mathrm{Ca}} \int_{\Gamma^n} \left(2\Delta_s^n H^n + \left(H^n\right)^3\right) \boldsymbol{n}^n \cdot \boldsymbol{v} = \int_{\Sigma_N} \boldsymbol{\sigma}^n \boldsymbol{n}^n \cdot \boldsymbol{v}, \qquad \forall \boldsymbol{v} \in \mathbb{V}(0), \tag{3.1}$$

$$\int_{\Lambda} q \, \mathrm{div} \, \boldsymbol{u}^n = 0, \qquad \forall q \in \mathbb{Q}, \tag{3.2}$$

$$\int_{\Gamma^n} \xi \, \mathrm{div}_s^n \, \boldsymbol{u}^n = 0, \qquad \forall \xi \in \mathbb{W}, \tag{3.3}$$

$$\int_{\Lambda} \frac{3\varphi^n - 4\varphi^{n-1} + \varphi^{n-2}}{2\Delta t} \psi + \int_{\Lambda} \left(\boldsymbol{u}^n \cdot \nabla \varphi^n\right) \psi = 0, \qquad \forall \psi \in \mathbb{X}(0). \tag{3.4}$$

The surface operators depend on the level set function φ, and the notation $\mathrm{div}_s^n \, \boldsymbol{v}$ stands for $\left(\mathbf{Id} - \boldsymbol{n}^n \otimes \boldsymbol{n}^n\right) : \nabla \boldsymbol{v}$. Analogously, the notations Δ_s^n and ∇_s^n are introduced for the discretized Laplace–Beltrami and surface gradient operators. Let $\Xi \equiv (\boldsymbol{u}, p, \lambda, \varphi)^T$ represent the global vector of unknowns, while $\Phi \equiv (\boldsymbol{v}, q, \xi, \psi)^T$ is the corresponding global vector of test functions. Let the operator $\mathscr{R}\left(\Xi^T\right)$ be the global residual vector. Therefore, the problem $\mathscr{P}^n$ consists in finding Ξ^n at time step t^n such that:

$$\left\langle \mathscr{R}\left(\Xi^{T,n}\right), \Phi^T \right\rangle \equiv \left(\langle \mathscr{R}_\Xi\left(\Xi^{T,n}\right), \boldsymbol{v}\rangle_{\mathbb{V}(0)',\mathbb{V}(0)}, \langle \mathscr{R}_p(\boldsymbol{u}^n), q\rangle_{\mathbb{Q}',\mathbb{Q}}, \langle \mathscr{R}_\lambda(\boldsymbol{u}^n), \xi\rangle_{\mathbb{W}',\mathbb{W}}, \langle \mathscr{R}_{\boldsymbol{u},\varphi}(\boldsymbol{u}^n, \varphi^n), \psi\rangle_{\mathbb{X}(0)',\mathbb{X}(0)}\right)^T$$
$$= \mathbf{0}, \quad \forall \Phi.$$

Analogously, a fully implicit time discretization scheme using BDF2 is adopted for the surface tension problem.

3.2. Inexact Newton methods

The Newton algorithm reduces the nonlinear problem $\mathscr{P}^n : \mathscr{R}\left(\Xi^T\right) = \mathbf{0}$ into a sequence of linear sub-problems. Given the numerical results at time instants $t \leqslant t^{n-1}$, we compute iteratively the solution Ξ_k^n at the following time t^n by a nonlinear Richardson method (loop over k). Indeed, for any sub-iteration $k \geqslant 1$, we look for the increments $\delta \Xi_k^n \equiv \left(\delta \boldsymbol{u}_k^n; \delta p_k^n, \delta \lambda_k^n, \delta \varphi_k^n\right)$ such that:

$$\left\langle D\mathscr{R}\left(\Xi_k^{T,n}\right)\left[\delta \Xi_k^{T,n}\right], \Phi \right\rangle = -\left\langle \mathscr{R}\left(\Xi_k^{T,n}\right), \Phi \right\rangle, \qquad \forall \Phi,$$

where $D\mathscr{R}\left(\Xi_k^{T,n}\right)$ represents the Gâteaux derivative of $\mathscr{R}$, see Appendix A. Hence, the Jacobian matrix of the coupled interface/fluid problem has a block-structure given by the derivatives of the global residual vector with respect to the global unknowns. The solution is explicitly updated on the k-th iteration of the nonlinear Richardson method (possibly using a relaxation parameter) such that $\Xi_{k+1}^n = \Xi_k^n + \delta \Xi_k^n$. We proceed subsequently with the next iteration.

Assuming $\Xi_{-1}^n = \Xi_0^n$, a second order extrapolation of the solution of the previous time steps enables to assign the starting values at each Newton loop. The method is applied recursively until the stopping criteria based on the computation of the global residual is satisfied. The Newton tolerance is set to 10^{-10} in our computations. It is worth pointing out that the tangent system is derived from the time discrete problem, therefore it depends on the time discretization scheme. We introduce the weighted multi-linear forms:

$$a(\boldsymbol{u}, \boldsymbol{v}; w) = \int_{\Lambda} 2w \, \mathbf{D}(\boldsymbol{u}) : \mathbf{D}(\boldsymbol{v}); \quad b(\boldsymbol{u}, q; \mathbf{T}) = -\int_{\Lambda} q \, \nabla \boldsymbol{u} : \mathbf{T}; \quad c(\boldsymbol{u}, \boldsymbol{v}; w, \boldsymbol{w}) = \int_{\Lambda} w \left((\boldsymbol{u} \cdot \nabla) \, \boldsymbol{w} + (\boldsymbol{w} \cdot \nabla) \, \boldsymbol{u}\right) . \boldsymbol{v};$$

$$d(\varphi, \boldsymbol{v}; w) = \int_{\Lambda} w \nabla \varphi \cdot \boldsymbol{v}; \quad e(\varphi, \psi; w) = \int_{\Lambda} w \, \varphi \psi; \quad f(\varphi, \psi; \mathbf{T}) = \int_{\Lambda} (\mathbf{T} \nabla \varphi) \cdot \nabla \psi; \quad m(\boldsymbol{u}, \boldsymbol{v}; w) = \int_{\Lambda} w \, \boldsymbol{u} \cdot \boldsymbol{v};$$

$$g(\varphi, \boldsymbol{v}; \boldsymbol{w}) = \int_{\Lambda} \varphi \boldsymbol{v} \cdot \boldsymbol{w}; \quad h(\varphi, \boldsymbol{v}; w, \boldsymbol{w}) = \int_{\Lambda} 2\varphi w \, \mathbf{D}(\boldsymbol{v}) : \mathbf{D}(\boldsymbol{w}); \quad k(\varphi, \boldsymbol{v}; \boldsymbol{w}, \mathbf{T}) = \int_{\Lambda} (\boldsymbol{w} \cdot \nabla \varphi) \, (\mathbf{T} : \nabla \boldsymbol{v});$$

$$l(\varphi, \boldsymbol{v}; \boldsymbol{w}, \mathbf{T}) = \int_{\Lambda} \left((\mathbf{T} \cdot \nabla \varphi) \otimes \boldsymbol{w} + \boldsymbol{w} \otimes (\mathbf{T} \cdot \nabla \varphi)\right) : \nabla \boldsymbol{v}; \quad j(\varphi, \psi; \boldsymbol{w}, \tilde{\boldsymbol{w}}, \mathbf{T}) = l(\varphi, \boldsymbol{w}; \psi \tilde{\boldsymbol{w}}, \mathbf{T});$$

$$i(\varphi, \psi; \boldsymbol{w}) = \int_{\Lambda} \psi \boldsymbol{w} \cdot \nabla \varphi; \quad n(\varphi, \psi; \boldsymbol{w}, \tilde{\boldsymbol{w}}) = \int_{\Lambda} \left(\boldsymbol{w} \cdot \nabla \varphi\right)\left(\tilde{\boldsymbol{w}} \cdot \nabla \psi\right),$$

defined for all scalar fields $q \in \mathbb{Q}$, $w \in L^\infty(\Lambda)$, $\varphi, \psi \in \mathbb{X}$; vectors $\boldsymbol{u}, \boldsymbol{v}, \boldsymbol{w}, \tilde{\boldsymbol{w}} \in \mathbb{V}$; and tensors $\mathbf{T} \in (L^\infty(\Lambda))^{2 \times 2}$.

In what follows, we will drop the superscript n referring to the time and we rather note k, referring to the Newton iteration, as a superscript, whenever it is clear from the context.

3.2.1. The surface tension problem

We first provide the exact derivation of the tangent system, which subsequently allows to validate the choice of the appropriate inexact Newton strategy. Let us introduce a mixed variable $\Psi \equiv H$ and we proceed with its computation in the weak sense to decrease the derivation order. Details about the linearization of the full problem in the direction of $\delta\Xi^T$ are provided in Appendix A. To compute the increment $\delta\Psi$, we proceed in a variational manner, and we have:

$$\left\langle \mathscr{R}_\Psi\left(\Psi,\varphi\right),\xi \right\rangle_{\mathbb{X}',\mathbb{X}} \equiv \int_\Lambda \Psi\xi + \int_\Lambda \frac{\nabla\varphi}{|\nabla\varphi|} \cdot \nabla\xi = 0, \qquad \forall \xi \in \mathbb{X}.$$

Using the equation $D\boldsymbol{n}[\delta\varphi] = \frac{\nabla_s \delta\varphi}{|\nabla\varphi|}$ derived in Appendix A, we obtain the following equation for the increment $\delta\Psi$:

$$\int_\Lambda \delta\Psi\xi + \int_\Lambda \frac{\nabla_s\delta\varphi}{|\nabla\varphi|} \cdot \nabla\xi = -\left\langle \mathscr{R}_\Psi\left(\Psi,\varphi\right),\xi \right\rangle_{\mathbb{X}',\mathbb{X}}, \qquad \forall \xi \in \mathbb{X}.$$

To introduce the tangent system, let us first express the corresponding residuals:

$$\left\langle \mathscr{R}_\Xi\left(\Xi^{T,k}\right),\boldsymbol{v} \right\rangle_{\mathbb{V}(\boldsymbol{0})',\mathbb{V}(\boldsymbol{0})} = \operatorname{Re} m\left(\frac{3\boldsymbol{u}^k - 4\boldsymbol{u}^{n-1} + \boldsymbol{u}^{n-2}}{2\Delta t}, \boldsymbol{v}; \rho_\varepsilon\left(\varphi^k\right)\right) + \frac{\operatorname{Re}}{2} c\left(\boldsymbol{u}^k, \boldsymbol{v}; \rho_\varepsilon\left(\varphi^k\right), \boldsymbol{u}^k\right)$$

$$+ a\left(\boldsymbol{u}^k, \boldsymbol{v}; \mu_\varepsilon\left(\varphi^k\right)\right) + b\left(\boldsymbol{v}, p^k; \mathbf{Id}\right) - \frac{1}{\operatorname{Ca}} d\left(\varphi^k, \boldsymbol{v}; \Psi^k \delta_\varepsilon\left(\varphi^k\right)\right) - \operatorname{Re} m\left(\boldsymbol{g}, \boldsymbol{v}; \rho_\varepsilon\left(\varphi^k\right)\right),$$

$$\left\langle \mathscr{R}_p\left(\boldsymbol{u}^k\right),q \right\rangle_{\mathbb{Q}',\mathbb{Q}} = b\left(\boldsymbol{u}^k, q; \mathbf{Id}\right),$$

$$\left\langle \mathscr{R}_\Psi\left(\Psi^k,\varphi^k\right),\xi \right\rangle_{\mathbb{X}',\mathbb{X}} = e\left(\Psi^k, \xi; 1\right) + f\left(\varphi^k, \xi; |\nabla\varphi^k|^{-1}\mathbf{Id}\right),$$

$$\left\langle \mathscr{R}_\varphi\left(\varphi^k,\boldsymbol{u}^k\right),\psi \right\rangle_{\mathbb{X}(0)',\mathbb{X}(0)} = e\left(\frac{3\varphi^k - 4\varphi^{n-1} + \varphi^{n-2}}{2\Delta t}, \psi; 1\right) + d\left(\varphi^k, \boldsymbol{u}^k; \psi\right),$$

for all $\boldsymbol{v} \in \mathbb{V}(\boldsymbol{0})$, $q \in \mathbb{Q}$, $\varphi \in \mathbb{X}$ and $\psi \in \mathbb{X}(0)$. The tangent system associated to the capillary problem (2.10), (2.7), (2.9) reads:

Given Ξ^k, find $\delta\Xi^k \equiv \left(\delta\boldsymbol{u}^k, \delta p^k, \delta\Psi^k, \delta\varphi^k\right) \in \mathbb{V}(\boldsymbol{u}_b) \times \mathbb{Q} \times \mathbb{X} \times \mathbb{X}(\varphi_b)$ such that

$$\operatorname{Re} m\left(\delta\boldsymbol{u}^k, \boldsymbol{v}; \frac{3\rho_\varepsilon(\varphi^k)}{2\Delta t}\right) + \operatorname{Re} c\left(\delta\boldsymbol{u}^k, \boldsymbol{v}; \rho_\varepsilon(\varphi^k), \boldsymbol{u}^k\right) + a\left(\delta\boldsymbol{u}^k, \boldsymbol{v}; \mu_\varepsilon\left(\varphi^k\right)\right) + b\left(\boldsymbol{v}, \delta p^k; \mathbf{Id}\right)$$

$$+ \operatorname{Re}\left(1 - \rho^\star\right) g\left(\delta\varphi^k, \boldsymbol{v}; \delta_\varepsilon\left(\varphi^k\right)\left(\frac{3\boldsymbol{u}^k - 4\boldsymbol{u}^{n-1} + \boldsymbol{u}^{n-2}}{2\Delta t} + \boldsymbol{u}^k \cdot \nabla\boldsymbol{u}^k\right)\right) + \left(1 - \mu^\star\right) h\left(\delta\varphi^k, \boldsymbol{v}; \delta_\varepsilon\left(\varphi^k\right), \boldsymbol{u}^k\right)$$

$$- \operatorname{Re}\left(1 - \rho^\star\right) g\left(\delta\varphi^k, \boldsymbol{v}; \delta_\varepsilon\left(\varphi^k\right)\boldsymbol{g}\right) - \frac{1}{\operatorname{Ca}} g\left(\delta\Psi^k, \boldsymbol{v}; \delta_\varepsilon\left(\varphi^k\right)\nabla\varphi^k\right) - \frac{1}{\operatorname{Ca}} g\left(\delta\varphi^k, \boldsymbol{v}; \Psi^k \delta_\varepsilon'\left(\varphi^k\right)\nabla\varphi^k\right)$$

$$- \frac{1}{\operatorname{Ca}} d\left(\delta\varphi^k, \boldsymbol{v}; \Psi^k \delta_\varepsilon\left(\varphi^k\right)\right) = -\left\langle \mathscr{R}_\Xi\left(\Xi^{T,k}\right), \boldsymbol{v} \right\rangle_{\mathbb{V}(\boldsymbol{0})',\mathbb{V}(\boldsymbol{0})}, \tag{3.5}$$

$$b\left(\delta\boldsymbol{u}^k, q; \mathbf{Id}\right) = -\left\langle \mathscr{R}_p\left(\boldsymbol{u}^k\right), q \right\rangle_{\mathbb{Q}',\mathbb{Q}}, \tag{3.6}$$

$$e\left(\delta\Psi^k, \xi; 1\right) + f\left(\delta\varphi^k, \xi; \frac{1}{|\nabla\varphi^k|}\left(\mathbf{Id} - \boldsymbol{n}^k \otimes \boldsymbol{n}^k\right)\right) = -\left\langle \mathscr{R}_\Psi\left(\Psi^k,\varphi^k\right), \xi \right\rangle_{\mathbb{X}',\mathbb{X}}, \tag{3.7}$$

$$e\left(\delta\varphi^k, \psi; \frac{3}{2\Delta t}\right) + i\left(\delta\varphi^k, \psi; \boldsymbol{u}^k\right) + g\left(\psi, \delta\boldsymbol{u}^k; \nabla\varphi^k\right) = -\left\langle \mathscr{R}_\varphi\left(\varphi^k,\boldsymbol{u}^k\right), \psi \right\rangle_{\mathbb{X}(0)',\mathbb{X}(0)}. \tag{3.8}$$

Inexact Newton formulation for the capillary problem In this paragraph, we assume that the redistancing problem (2.5) is sufficiently solved until reaching the convergence. Therefore, the level set function φ tightly approaches a signed distance function, and we use the simplifying assumption $|\nabla\varphi| = 1$ everywhere in Λ to approximate the Jacobian matrix of the problem (yielding an inexact or quasi-Newton approach). Although the global convergence speed of the Newton algorithm can be deteriorated if the redistancing problem is not accurately solved until convergence, the latter approximation helps to simplify the force expression (and consequently the numerical assembly) at each Newton sub-iteration. This simplification appears to be more beneficial especially for the vesicle problem characterized by the high nonlinearities of the membrane force.

Details about the simplifications are provided in Appendix A. The tangent problem corresponding to the inexact approximation is given by the coupled system (3.5), (3.6), (3.8) and the equation

$$e\left(\delta\Psi^k, \xi; 1\right) + f\left(\delta\varphi^k, \xi; \mathbf{Id}\right) = -\left\langle \mathcal{R}_\Psi\left(\Psi^k, \varphi^k\right), \xi\right\rangle_{\mathbb{X}',\mathbb{X}}, \tag{3.9}$$

for all $(\boldsymbol{v}, q, \xi, \psi) \in \mathbb{V}(\boldsymbol{0}) \times \mathbb{Q} \times \mathbb{X} \times \mathbb{X}(0)$. The resulting inexact Newton scheme will be referred to as "QN1".

In addition, we consider a second simplification of the Newton scheme, referred to as "QN2", in which we disregard all shape derivative terms weighted by $\delta'_\varepsilon(\varphi)$ in the Jacobian matrix, see Eq. (3.5).

Note on the mass correction for the capillary problem A well-known problem related to the Eulerian methods is that they are not mass (or volume) conserving for divergence-free velocity fields. To address this issue, we use an approach analogous to that described in [31] where a posteriori mass correction term is considered in the advection equation (3.4). A forcing term is then introduced in (3.4) after the semi-discretization in time and acts as a constraint fixing the area $|\Omega^n| = |\Omega^0|$. At time t^n, let ζ^n represent a global Lagrange multiplier corresponding to the previous constraint. The advection velocity is then corrected in the normal direction and φ is instead advected with the vector $\boldsymbol{u} + \zeta\boldsymbol{n}$. Following [31], an a posteriori mass correction referred to as ς^n at any time t^n is also required, and the advection problem (2.4) is substituted by the system:

$$\frac{\partial\varphi}{\partial t} + (\boldsymbol{u} + \zeta\boldsymbol{n}) \cdot \nabla\varphi = 0 \quad \text{in } (0, T) \times \Lambda \qquad \text{and}$$

$$\frac{\mathrm{d}|\Omega|}{\mathrm{d}t}\left(t^n\right) = \left[\frac{\mathrm{d}}{\mathrm{d}t}\int_\Lambda \left(1 - \mathscr{H}_\varepsilon(\varphi)\right)\right]_{t=t^n} \approx \frac{3|\Omega^n| - 4|\Omega^{n-1}| + |\Omega^{n-2}|}{2\Delta t}.$$

The quantities $|\Omega^{n-1}|$ and $|\Omega^{n-2}|$ are known from the previous iterations, whereas we need to enforce the condition $|\Omega^n| = |\Omega^0|$. Let us introduce the term:

$$\varsigma^n = \frac{3|\Omega^0| - 4|\Omega^{n-1}| + |\Omega^{n-2}|}{2\Delta t}.$$

By using the equation (2.11), we obtain:

$$\frac{\mathrm{d}|\Omega|}{\mathrm{d}t} = \frac{\mathrm{d}}{\mathrm{d}t}\int_\Lambda \left(1 - \mathscr{H}_\varepsilon(\varphi)\right)\mathrm{d}\boldsymbol{x} = -\int_\Lambda \frac{\partial\varphi}{\partial t}\delta_\varepsilon(\varphi)\mathrm{d}\boldsymbol{x} = -\int_\Gamma \frac{1}{|\nabla\phi|}\frac{\partial\varphi}{\partial t}\mathrm{d}\boldsymbol{s} = \int_\Gamma \frac{1}{|\nabla\phi|}\left(\boldsymbol{u}.\nabla\varphi + \zeta|\nabla\phi|\right)\mathrm{d}\boldsymbol{s}$$

$$= \int_\Gamma \boldsymbol{u}.\boldsymbol{n}\,\mathrm{d}\boldsymbol{s} + \zeta|\Gamma|.$$

That results in an explicit expression of the forcing term ζ^n:

$$\zeta^n = \frac{1}{|\Gamma^n|}\left(\varsigma^n - \int_{\Gamma^n} \boldsymbol{u}^n.\boldsymbol{n}^n\,\mathrm{d}s\right) \approx \frac{1}{|\Gamma^n|}\left(\varsigma^n - \int_\Lambda \boldsymbol{u}^n.\nabla\varphi^n\,\mathrm{d}x\right).$$

3.2.2. The vesicle problem

To state the appropriate weak formulation for the vesicle problem $\mathscr{P}^n$, we keep calling the mixed variable $\Psi = H$ and we introduce a second mixed variable $\Phi = \Delta_s\Psi$. Hence, the global vector of unknowns associated with the full problem $\mathscr{P}^n$ (3.1), (3.2), (3.3), (3.4) reads $\boldsymbol{\Xi}^k \equiv (\boldsymbol{u}^k, p^k, \lambda^k, \Phi^k, \Psi^k, \varphi^k)^T$, while the tangent problem depends on the global increment $\delta\boldsymbol{\Xi}^k \equiv (\delta\boldsymbol{u}^k, \delta p^k, \delta\Phi^k, \delta\Psi^k, \delta\varphi^k)^T$ at the Newton subiteration k.

Using the expressions provided in Appendix A, the directional derivative of the inextensibility constraint (2.8) in the direction of $\delta\boldsymbol{\Xi}$ is obtained after performing the regularization in accordance with (2.11). We obtain:

$$D \operatorname{div}_s \boldsymbol{u} \, |\nabla\varphi|\delta_\varepsilon(\varphi)[\delta\boldsymbol{\Xi}] \equiv D\left(\operatorname{div}\boldsymbol{u} - (\boldsymbol{n}\cdot\nabla\boldsymbol{u})\cdot\boldsymbol{n}\right)|\nabla\varphi|\delta_\varepsilon(\varphi)[\delta\boldsymbol{\Xi}]$$

$$= \operatorname{div}_s \delta\boldsymbol{u} \, |\nabla\varphi|\delta_\varepsilon(\varphi) + \operatorname{div}_s \boldsymbol{u} \, \delta_\varepsilon(\varphi)\frac{\nabla\varphi}{|\nabla\varphi|}\cdot\nabla\delta\varphi + \operatorname{div}_s \boldsymbol{u} \, |\nabla\varphi|\delta'_\varepsilon(\varphi)\delta\varphi$$

$$- \left(\left(\frac{\nabla_s\delta\varphi}{|\nabla\varphi|}\cdot\nabla\boldsymbol{u}\right)\cdot\frac{\nabla\varphi}{|\nabla\varphi|} + \left(\frac{\nabla\varphi}{|\nabla\varphi|}\cdot\nabla\boldsymbol{u}\right)\cdot\frac{\nabla_s\delta\varphi}{|\nabla\varphi|}\right)|\nabla\varphi|\delta_\varepsilon(\varphi).$$

The derivative of the dimensionless and regularized force of Canham–Helfrich–Evans $\boldsymbol{F}_\Gamma$ (2.3) reads:

$$2\mathrm{Ca}\, D\boldsymbol{F}_\Gamma\, |\nabla\varphi|\delta_\varepsilon\,(\varphi)\,[\delta\,\boldsymbol{\Xi}] \equiv D\left(2\Delta_s H + H^3\right)|\nabla\varphi|\delta_\varepsilon\,(\varphi)\,\boldsymbol{n}[\delta\,\boldsymbol{\Xi}] = D\left(2\Phi + \Psi^3\right)\delta_\varepsilon\,(\varphi)\,\nabla\varphi[\delta\,\boldsymbol{\Xi}]$$

$$= \left(2\delta\Phi + 3\Psi^2\delta\Psi\right)\delta_\varepsilon\,(\varphi)\,\nabla\varphi + \left(2\Phi + \Psi^3\right)\delta_\varepsilon\,(\varphi)\,\nabla\delta\varphi + \left(2\Phi + \Psi^3\right)\delta_\varepsilon'\,(\varphi)\,\delta\varphi\,\nabla\varphi.$$

Analogously to (3.7), we compute $\delta\Phi$. Let us introduce φ_m and φ_M such that $\varphi \in [\varphi_m, \varphi_M]$. Thanks to the co-area formula [58], we obtain:

$$\int_\Lambda |\nabla\varphi|\Phi\,\phi\,\mathrm{d}\mathbf{x} = \int_{\varphi_m}^{\varphi_M}\left(\int_{\varphi=z}\Delta_s\Psi\phi\,\mathrm{d}\mathbf{s}\right)\mathrm{d}\mathbf{z} = \int_{\varphi_m}^{\varphi_M}\left(-\int_{\varphi=z}\nabla_s\Psi\cdot\nabla_s\phi\,\mathrm{d}\mathbf{s} + \int_{\varphi=z}\phi\Psi\underbrace{\boldsymbol{n}\cdot\nabla_s\Psi}_{0}\,\mathrm{d}\mathbf{s}\right)\mathrm{d}\mathbf{z}$$

yielding the equation:

$$\left\langle\mathscr{R}_\Phi\,(\Phi,\Psi,\varphi)\,,\phi\right\rangle_{\mathbb{X}',\mathbb{X}} \equiv \int_\Lambda |\nabla\varphi|\Phi\phi + \int_\Lambda |\nabla\varphi|\nabla_s\Psi\cdot\nabla\phi = 0, \qquad \forall\phi\in\mathbb{X}.$$

The latter equation holds thanks to the following relation verified by the surface projection operator $\mathbf{Id} - \boldsymbol{n}\otimes\boldsymbol{n} = (\mathbf{Id} - \boldsymbol{n}\otimes\boldsymbol{n})^T = (\mathbf{Id} - \boldsymbol{n}\otimes\boldsymbol{n})^2$. The increment $\delta\Phi$ verify then the following equation:

$$\int_\Lambda |\nabla\varphi|\delta\Phi\,\phi + \int_\Lambda\left(\Phi\phi + \nabla_s\Psi\cdot\nabla\phi\right)\nabla\delta\varphi\cdot\frac{\nabla\varphi}{|\nabla\varphi|} + \int_\Lambda |\nabla\varphi|\nabla_s\delta\Psi\cdot\nabla\phi$$

$$- \int_\Lambda (\nabla_s\delta\varphi\cdot\nabla\Psi)\left(\frac{\nabla\varphi}{|\nabla\varphi|}\cdot\nabla\phi\right) - \int_\Lambda\left(\frac{\nabla\varphi}{|\nabla\varphi|}\cdot\nabla\Psi\right)(\nabla_s\delta\varphi\cdot\nabla\phi) = -\langle\mathscr{R}_\Phi\,(\Phi,\Psi,\varphi)\,,\phi\rangle_{\mathbb{X}',\mathbb{X}}, \quad \forall\phi\in\mathbb{X}.$$

Analogously to the capillary Problem 3.2.1, a posteriori mass correction $\varsigma(t^n)$ for the area and perimeter is considered in the vesicle problem. We use the same strategy described in [31, section 3.3.2], in which two corrections are considered in the level set equation (2.9) and act as forcing terms fixing the incompressibility and inextensibility constraints $\left|\Omega(t^n)\right| = \left|\Omega(t=0)\right|$ and $\left|\Gamma(t^n)\right| = \left|\Gamma(t=0)\right|$.

For ease of exposition, the exact tangent system associated with the vesicle problem $\mathscr{P}^n$ (3.1), (3.2), (3.3), (3.4) is postponed to Appendix B. At the numerical level, that corresponds to an exact Jacobian matrix in the linear system.

Inexact Newton strategy with the simplifying signed distance assumption In the rising bubble Example 4.1, we clearly observe that the quadratic convergence of the exact Newton is slightly affected when considering the inexact Jacobian matrix under the simplifying assumption of a signed distance function $\left|\nabla\varphi\right| = 1$ everywhere in Λ. An accurate resolution of the redistancing problem until convergence is then required, especially in the vicinity of the membrane Γ. From Appendix A, we remark that the assumption $\left|\nabla\varphi\right| = 1$ induces the equation $\boldsymbol{n}\cdot\nabla\delta\varphi = 0$ in Λ.

For ease of exposition, we only present the weak formulation in the particular case $\rho^\star = 1$, assumed afterwards for the simulation of vesicles under simple shear flow [26,31]. Consequently, an inexact Newton strategy is obtained and the tangent system associated to the vesicle problem $\mathscr{P}^n$ simply reads:

Given $\boldsymbol{\Xi}^k$, find the increment $\delta\boldsymbol{\Xi}^k \equiv \left(\delta\boldsymbol{u}^k, \delta p^k, \delta\lambda^k, \delta\Phi^k, \delta\Psi^k, \delta\varphi^k\right) \in \mathbb{V}(\boldsymbol{u}_b)\times\mathbb{Q}\times\mathbb{Q}\times\mathbb{X}\times\mathbb{X}\times\mathbb{X}(\varphi_b)$ such that

$$\frac{\mathrm{Re}}{\Delta t}m\left(\delta\boldsymbol{u}^k, \boldsymbol{v}; \frac{3}{2}\right) + \mathrm{Re}\,c\left(\delta\boldsymbol{u}^k, \boldsymbol{v}; 1, \boldsymbol{u}^k\right) + a\left(\delta\boldsymbol{u}^k, \boldsymbol{v}; \mu_\varepsilon\left(\varphi^k\right)\right) + b\left(\boldsymbol{v}, \delta p^k; \mathbf{Id}\right)$$

$$+ (1-\mu^\star)h\left(\delta\varphi^k, \boldsymbol{v}; \delta_\varepsilon\left(\varphi^k\right), \boldsymbol{u}^k\right)$$

$$+ b\left(\boldsymbol{v}, \delta\lambda^k; \delta_\varepsilon\left(\varphi^k\right)\left(\mathbf{Id} - \nabla\varphi^k\otimes\nabla\varphi^k\right)\right) + b\left(\boldsymbol{v}, \delta\varphi^k; \lambda^k\delta_\varepsilon'\left(\varphi^k\right)\left(\mathbf{Id} - \nabla\varphi^k\otimes\nabla\varphi^k\right)\right)$$

$$- \frac{1}{\mathrm{Ca}}g\left(\delta\Phi^k, \boldsymbol{v}; \delta_\varepsilon\left(\varphi^k\right)\nabla\varphi^k\right)$$

$$+ l\left(\delta\varphi^k, \boldsymbol{v}; \lambda^k\delta_\varepsilon\left(\varphi^k\right)\nabla\varphi^k, \mathbf{Id}\right) - \frac{3}{2\mathrm{Ca}}g\left(\delta\Psi^k, \boldsymbol{v}; \left(\Psi^k\right)^2\delta_\varepsilon\left(\varphi^k\right)\nabla\varphi^k\right)$$

$$- \frac{1}{2\mathrm{Ca}} d\left(\delta\varphi^k, \boldsymbol{v}; \left(2\Phi^k + \left(\Psi^k\right)^3\right) \delta_\varepsilon\left(\varphi^k\right)\right)$$

$$- \frac{1}{2\mathrm{Ca}} g\left(\delta\varphi^k, \boldsymbol{v}; \left(2\Phi^k + \left(\Psi^k\right)^3\right) \delta'_\varepsilon\left(\varphi^k\right) \nabla\varphi^k\right) = -\langle\mathscr{R}_{\boldsymbol{\Xi}}\left(\boldsymbol{\Xi}^{T,k}\right), \boldsymbol{v}\rangle_{\mathbb{V}(\boldsymbol{0})', \mathbb{V}(\boldsymbol{0})}, \tag{3.10}$$

$$b\left(\delta\boldsymbol{u}^k, q; \mathbf{Id}\right) = -\langle\mathscr{R}_p\left(\boldsymbol{u}^k\right), q\rangle_{\mathbb{Q}', \mathbb{Q}}, \tag{3.11}$$

$$b\left(\delta\boldsymbol{u}^k, \eta; \delta_\varepsilon\left(\varphi^k\right)\left(\mathbf{Id} - \nabla\varphi^k \otimes \nabla\varphi^k\right)\right) - e\left(\delta\varphi^k, \eta; \delta'_\varepsilon\left(\varphi^k\right)\left(\mathbf{Id} - \nabla\varphi^k \otimes \nabla\varphi^k\right) : \nabla\boldsymbol{u}^k\right)$$

$$+ j\left(\delta\varphi^k, \eta; \boldsymbol{u}^k, \delta_\varepsilon\left(\varphi^k\right)\nabla\varphi^k, \mathbf{Id}\right) = -\langle\mathscr{R}_\lambda\left(\boldsymbol{u}^k\right), \eta\rangle_{\mathbb{Q}', \mathbb{Q}}, \tag{3.12}$$

$$e\left(\delta\Phi^k, \phi; 1\right) + f\left(\delta\Psi^k, \phi; \mathbf{Id} - \nabla\varphi^k \otimes \nabla\varphi^k\right) - n\left(\delta\varphi^k, \phi; \nabla\Psi^k, \nabla\varphi^k\right)$$

$$- f\left(\delta\varphi^k, \phi; \left(\nabla\varphi^k \cdot \nabla\Psi^k\right)\mathbf{Id}\right) = -\langle\mathscr{R}_\Phi\left(\Phi^k, \Psi^k, \varphi^k\right), \phi\rangle_{\mathbb{X}', \mathbb{X}}, \tag{3.13}$$

$$e\left(\delta\Psi^k, \xi; 1\right) + f\left(\delta\varphi^k, \xi; \mathbf{Id}\right) = -\langle\mathscr{R}_\Psi\left(\Psi^k, \varphi^k\right), \xi\rangle_{\mathbb{X}', \mathbb{X}}, \tag{3.14}$$

$$e\left(\delta\varphi^k, \psi; \frac{3}{2\Delta t}\right) + i\left(\delta\varphi^k, \psi; \boldsymbol{u}^k\right) + g\left(\psi, \delta\boldsymbol{u}^k; \nabla\varphi^k\right) = -\langle\mathscr{R}_\varphi\left(\varphi^k, \boldsymbol{u}^k\right), \psi\rangle_{\mathbb{X}(0)', \mathbb{X}(0)}, \tag{3.15}$$

for all test functions $(\boldsymbol{v}, q, \eta, \phi, \xi, \psi) \in \mathbb{V}(\boldsymbol{0}) \times \mathbb{Q} \times \mathbb{Q} \times \mathbb{X} \times \mathbb{X} \times \mathbb{X}(0)$.

Note on the time step size for the vesicle problem We here focus on the choice of the time step size for the vesicle problem. The convergence of the Newton algorithm is very sensitive to the time step Δt because too large values may lead to starting values which are far from the expected solutions, see Section 4.2. Indeed, the Newton method has only local convergence properties and there exist several strategies that enable to improve the choice of the starting values but that is beyond the scope of the present work. We then proceed with an adaptation strategy for the time step Δt to ensure the convergence of the Newton subiterations. Therefore, we decrease the size Δt by a factor $1/2$ if the Newton loop does not converge within 10 iterations. The problem is then solved again using the values of $\boldsymbol{u}$ and φ at the previous time steps t_{n-1} and t_{n-2} but using the reduced time step size. However, if the Newton loop converges, the time step size is increased for the next time step by an amplification factor equal to 1.2, see Subsection 4.3.

Remark that, by considering the adaptive time step size, the adaptive step size BDF2 has a different expression, see [59]. More precisely, the time derivative terms are rather approximated by:

$$\frac{\partial\boldsymbol{u}}{\partial t} \approx \frac{(1+2\vartheta_n)\,\boldsymbol{u}^{n+2} - (1+\vartheta_n)^2\,\boldsymbol{u}^{n+1} + \vartheta_n^2\boldsymbol{u}^n}{(1+\vartheta_n)\,\Delta t_2} \quad \text{and} \quad \frac{\partial\varphi}{\partial t} \approx \frac{(1+2\vartheta_n)\,\varphi^{n+2} - (1+\vartheta_n)^2\,\varphi^{n+1} + \vartheta_n^2\varphi^n}{(1+\vartheta_n)\,\Delta t_2},$$

with $\Delta t_2 = t_{n+2} - t_{n+1}$, $\Delta t_1 = t_{n+1} - t_n$ and $\vartheta_n = \Delta t_2 / \Delta t_1$.

For ease of exposition, the vesicle problem is only presented using the constant step size formula.

3.3. Finite element space discretization

Let us consider a partition $\mathscr{T}$ of Λ consisting of geometrically conforming open simplicial elements K (triangles in 2D), such that $\overline{\Lambda} = \underset{K \in \mathscr{T}}{\cup}$. For all $K \in \mathscr{T}$, the diameter of K is denoted h_K, and we define the mesh size as the largest mesh element diameter $h = \max_{K \in \mathscr{T}_h} h_K$. Let $\mathscr{T}_h$ denote a mesh $\mathscr{T}$ having a mesh size h. We consider a Taylor–Hood finite element approximation [60] for the approximation of the velocity and pressure, while the same approximation for pressure is used for the Lagrange multiplier corresponding to the inextensibility constraint [31]. A high-order finite element approximation is used for the level set function φ. Let us denote by $\boldsymbol{u}^n_{k,h}$ an approximation of $\boldsymbol{u}^n_k$ at the k-th Newton iteration of time t_n. Analogously, similar notations are used for the other fields. To proceed with the fully discrete variant of the problem (3.10)–(3.11)–(3.12)–(3.13)–(3.14)–(3.15), we first have a close look on the corresponding structure of the matrix of the linear system. The system has a sparse block structure which is singular, since the inextensibility constraint and the corresponding regularized Lagrange multiplier have a non-zero values only in the banded strip of width 2ε in the surrounding of Γ. Accordingly, the use of a direct solver is ruled out. To address this issue, we use the so-called banded level set approach that consists in assembling only the non-zero coefficients in the global matrix of the linear system. Further details about this technique can be found in [44,61]. We then introduce the banded domain $B_{h,\varepsilon}(t) = \left\{K \in \mathscr{T}_h : \delta_\varepsilon\left(\varphi\right) \neq 0\right\}$. We consider the following finite dimensional spaces:

$$\mathbb{V}_h(\boldsymbol{u}_b) = \left\{\boldsymbol{u} \in \mathbb{V}(\boldsymbol{u}_b) \cap C^0\left(\overline{\Lambda}\right)^2, \boldsymbol{u}_{|K} \in (\mathbb{P}_2(K))^2, \forall K \in \mathscr{T}_h\right\}, \qquad \mathbb{X}_h = \left\{\varphi \in C^0\left(\overline{\Lambda}\right), \varphi_{|K} \in \mathbb{P}_2(K), \forall K \in \mathscr{T}_h\right\},$$

$$\mathbb{Q}_h = \left\{q \in \mathbb{Q} \cap C^0\left(\overline{\Lambda}\right), q_{|K} \in \mathbb{P}_1(K), \forall K \in \mathscr{T}_h\right\} \quad \text{and} \quad \mathbb{W}_{h,\varepsilon} = \left\{\lambda \in L^2(B_{h,\varepsilon}) \cap C^0(\overline{\Lambda}) : \lambda_{|K} \in \mathbb{P}_1, \forall K \in B_{h,\varepsilon}\right\}.$$

For a given regular weights $w, \hat{w}, \tilde{w}, \boldsymbol{w}, \tilde{\boldsymbol{w}}, \hat{\boldsymbol{w}}, \mathbf{T}$ adequately corresponding to (3.10)–(3.11)–(3.12)–(3.13)–(3.14)–(3.15), we define the bounded weighted linear operators $\mathcal{A} : \mathbb{V}_h(\boldsymbol{u}_b) \rightarrow \mathbb{V}'_h(\mathbf{0})$, $\mathcal{B} : \mathbb{Q}_h \rightarrow \mathbb{V}'_h(\mathbf{0})$, $\mathcal{C} : \mathbb{W}_{h,\varepsilon} \rightarrow \mathbb{V}'_h(\mathbf{0})$, $\mathcal{D} : \mathbb{X}_h \rightarrow \mathbb{V}'_h(\mathbf{0})$, $\mathcal{E} : \mathbb{X}_h \rightarrow \mathbb{V}'_h(\mathbf{0})$, $\mathcal{F} : \mathbb{X}_h \rightarrow \mathbb{V}'_h(\mathbf{0})$, $\mathcal{G} : \mathbb{X}_h \rightarrow \mathbb{W}'_{h,\varepsilon}$, $\mathcal{H} : \mathbb{X}_h \rightarrow \mathbb{X}'_h$, $\mathcal{I} : \mathbb{X}_h \rightarrow \mathbb{X}'_h$, $\mathcal{J} : \mathbb{X}_h \rightarrow \mathbb{X}'_h$, $\mathcal{K} : \mathbb{X}_h \rightarrow \mathbb{X}'_h$, $\mathcal{L} : \mathbb{X}_h \rightarrow \mathbb{X}'_h$, $\mathcal{M} : \mathbb{V}_h(\boldsymbol{u}_b) \rightarrow \mathbb{X}'_h$, $\mathcal{N} : \mathbb{X}_h \rightarrow \mathbb{X}'_h$, as follows:

$$\langle \mathcal{A}(\boldsymbol{u}), \boldsymbol{v} \rangle = m(\boldsymbol{u}, \boldsymbol{v}; w) + c(\boldsymbol{u}, \boldsymbol{v}; \hat{w}, \boldsymbol{w}) + a(\boldsymbol{u}, \boldsymbol{v}; \tilde{w}), \quad \langle \mathcal{B}(p), \boldsymbol{v} \rangle = b(\boldsymbol{v}, p; \mathbf{Id}), \quad \langle \mathcal{C}(\lambda), \boldsymbol{v} \rangle = b(\boldsymbol{v}, \lambda; \mathbf{T}),$$

$$\langle \mathcal{D}(\varphi), \boldsymbol{v} \rangle = b(\boldsymbol{v}, \varphi; \mathbf{Id}) + h(\varphi, \boldsymbol{v}; w) + l(\varphi, \boldsymbol{v}; \tilde{\boldsymbol{w}}, \mathbf{Id}) + d(\varphi, \boldsymbol{v}; w) + g(\varphi, \boldsymbol{v}; \hat{\boldsymbol{w}}), \quad \langle \mathcal{E}(\Phi), \boldsymbol{v} \rangle = g(\Phi, \boldsymbol{v}; w),$$

$$\langle \mathcal{F}(\Psi), \boldsymbol{v} \rangle = g(\Psi, \boldsymbol{v}; w), \quad \langle \mathcal{G}(\varphi), \eta \rangle = e(\varphi, \eta; w) + j(\varphi, \eta; \boldsymbol{w}, \tilde{\boldsymbol{w}}, \mathbf{Id}), \quad \langle \mathcal{H}(\Psi), \phi \rangle = f(\Psi, \phi; \mathbf{Id}),$$

$$\langle \mathcal{I}(\varphi), \phi \rangle = n(\varphi, \phi; \boldsymbol{w}, \tilde{\boldsymbol{w}}) + f(\varphi, \phi; \mathbf{T}), \quad \langle \mathcal{J}(\Psi), \xi \rangle = e(\Psi, \xi; w), \quad \langle \mathcal{K}(\varphi), \xi \rangle = f(\varphi, \xi; \mathbf{Id}),$$

$$\langle \mathcal{L}(\varphi), \psi \rangle = e(\varphi, \psi; w) + i(\varphi, \psi; \boldsymbol{w}), \quad \langle \mathcal{M}(\boldsymbol{u}), \psi \rangle = g(\psi, \boldsymbol{u}; w), \quad \langle \mathcal{N}(\Phi), \phi \rangle = e(\Phi, \phi; 1),$$

for all $\boldsymbol{v} \in \mathbb{V}_h(\mathbf{0})$, $q \in \mathbb{Q}_h$, $\eta \in \mathbb{W}_{h,\varepsilon}$, $\phi \in \mathbb{X}_h$, $\xi \in \mathbb{X}_h$ and $\psi \in \mathbb{X}_h$. The Galerkin scheme associated to (3.10)–(3.11)–(3.12)–(3.13)–(3.14)–(3.15)) consists in finding $\delta \boldsymbol{\Xi}^n_{k,h} \equiv \left(\delta \boldsymbol{u}^n_{k,h}, \delta p^n_{k,h}, \delta \lambda^n_{k,h}, \delta \Phi^n_{k,h}, \delta \Psi^n_{k,h}, \delta \varphi^n_{k,h}\right) \in \mathbb{V}_h(\boldsymbol{u}_b) \times \mathbb{Q}_h \times \mathbb{W}_{h,\varepsilon} \times \mathbb{X}_h \times \mathbb{X}_h \times \mathbb{X}_h$ such that

$$\left\langle \mathcal{A}\left(\delta \boldsymbol{u}^n_{k,h}\right), \boldsymbol{v}_h \right\rangle + \left\langle \mathcal{B}\left(\delta p^n_{k,h}\right), \boldsymbol{v}_h \right\rangle + \left\langle \mathcal{C}\left(\delta \lambda^n_{k,h}\right), \boldsymbol{v}_h \right\rangle + \left\langle \mathcal{D}\left(\delta \varphi^n_{k,h}\right), \boldsymbol{v}_h \right\rangle + \left\langle \mathcal{E}\left(\delta \Phi^n_{k,h}\right), \boldsymbol{v}_h \right\rangle + \left\langle \mathcal{F}\left(\delta \Psi^n_{k,h}\right), \boldsymbol{v}_h \right\rangle$$

$$= -\left\langle \mathscr{R}_{\boldsymbol{\Xi}}\left(\boldsymbol{\Xi}^n_{k,h}\right), \boldsymbol{v}_h \right\rangle, \tag{3.16}$$

$$\left\langle q_h, \mathcal{B}'\left(\delta \boldsymbol{u}^n_{k,h}\right) \right\rangle = -\left\langle \mathscr{R}_p\left(\boldsymbol{u}^n_{k,h}\right), q_h \right\rangle, \tag{3.17}$$

$$\left\langle \eta_h, \mathcal{C}'\left(\delta \boldsymbol{u}^n_{k,h}\right) \right\rangle + \left\langle \mathcal{G}\left(\delta \varphi^n_{k,h}\right), \eta_h \right\rangle = -\left\langle \mathscr{R}_\lambda\left(\boldsymbol{u}^n_{k,h}, \varphi^n_{k,h}\right), \eta_h \right\rangle, \tag{3.18}$$

$$\left\langle \mathcal{N}\left(\delta \Phi^n_{k,h}\right), \phi_h \right\rangle + \left\langle \mathcal{H}\left(\delta \Psi^n_{k,h}\right), \phi_h \right\rangle + \left\langle \mathcal{I}\left(\delta \varphi^n_{k,h}\right), \phi_h \right\rangle = -\left\langle \mathscr{R}_\Phi\left(\Phi^n_{k,h}, \Psi^n_{k,h}, \varphi^n_{k,h}\right), \xi_h \right\rangle, \tag{3.19}$$

$$\left\langle \mathcal{J}\left(\delta \Psi^n_{k,h}\right), \xi_h \right\rangle + \left\langle \mathcal{K}\left(\delta \varphi^n_{k,h}\right), \xi_h \right\rangle = -\left\langle \mathscr{R}_\Psi\left(\Psi^n_{k,h}, \varphi^n_{k,h}\right), \xi_h \right\rangle, \tag{3.20}$$

$$\left\langle \mathcal{L}\left(\delta \varphi^n_{k,h}\right), \psi_h \right\rangle + \left\langle \mathcal{M}\left(\delta \boldsymbol{u}^n_{k,h}\right), \psi_h \right\rangle = -\left\langle \mathscr{R}_\varphi\left(\varphi^n_{k,h}, \boldsymbol{u}^n_{k,h}\right), \psi_h \right\rangle, \tag{3.21}$$

for all $(\boldsymbol{v}_h, q_h, \eta_h, \phi_h, \xi_h, \psi_h) \in \mathbb{V}_h(\mathbf{0}) \times \mathbb{Q}_h \times \mathbb{W}_{h,\varepsilon} \times \mathbb{X}_h \times \mathbb{X}_h \times \mathbb{X}_h$. We notice that, in practice, we only assemble the surface integral terms and the equations (3.19) and (3.20) in the banded region surrounding the membrane Γ. In fact, only these coefficients are needed to solve the vesicle problem, and this enables in addition to reduce the size of the global matrix of the linear system. Moreover, we remark that the variables $\delta \Phi^n_{k,h}$ and $\delta \Psi^n_{k,h}$ in (3.19) and (3.20) can be eliminated by inverting the mass matrix at the element level. Details are provided in Appendix C.

Regarding the finite element discretization of the redistancing problem (2.5), we notice that the evaluation of the right-hand-side involving the characteristics should be considered with care. The Gauss–Lobatto quadrature formula is used here, as it guaranties further stability of the characteristics method [62, sec. 1.11].

4. Numerical results and discussion

Software implementation　　All simulations have been implemented using the C++ library for scientific computing Rheolef [57], initially developed by the author P. Saramito. Rheolef provides support for distributed-memory parallelism via MPI.[1] It relies upon the Boost,[2] Blas,[3] and UMFPACK[4] libraries for much of its functionalities. It also bases on Scotch for distributed mesh partitioning.[5] Results are displayed graphically with the software Paraview,[6] whereas the tracings are generated with the software Gnuplot.[7]

---

[1]　Message Passing Interface – http://www.mpi-forum.org.
[2]　Boost libraries – http://www.boost.org.
[3]　Basic Linear Algebra Subprograms library – http://www.netlib.org/blas.
[4]　Umfpack routines – http://www.cise.ufl.edu/research/sparse/umfpack/.
[5]　Scotch – http://www.labri.fr/perso/pelegrin/scotch.
[6]　Paraview – http://www.paraview.org.
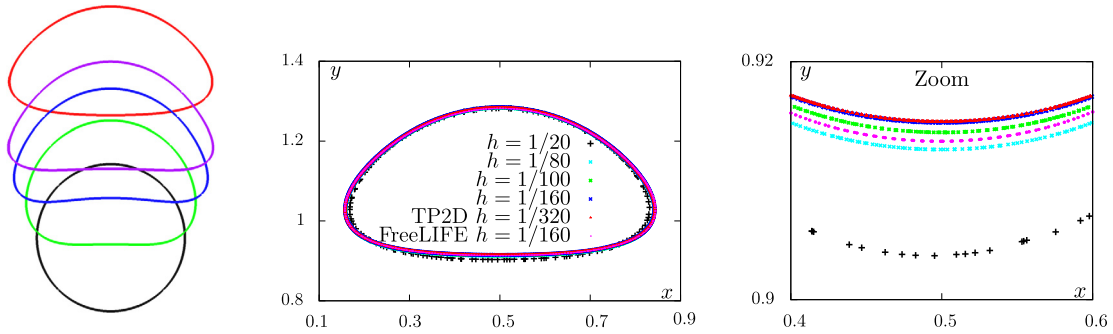[7]　Gnuplot – http://www.gnuplot.info.

Fig. 2. (left) Shapes of the rising bubble obtained with the finest mesh $h = 1/160$ (NTS $= 1'352$, NEL $= 135'110$) at different times $t \in \{0, 1, 1.5, 2, 3\}$. The display window corresponds to $[0.1, 0.9] \times [0.2, 1.3]$. (middle) Comparison of the final shapes with reference solutions at $T = 3$ [63]. (right) Close-up in zone of maximal disparities at $T = 3$ (same legend as middle).

4.1. Example 1: Quantitative benchmark of the rising bubble dynamics

The aims of this example are twofold. On the one hand, we perform numerical computations using the inexact Newton strategy QN1 previously devised in the case of the capillary forces. On the other hand, we investigate the convergence properties of the inexact Newton strategies with respect to the exact Newton method. In this regard, we check the accuracy of our solver in the context of the rising bubble benchmark introduced in Hysing et al. [63]. We emphasize that all simulations will be performed using the inexact Newton strategy QN1, unless otherwise stated.

Let us consider the set-up of the ellipsoidal bubble characterized by the physical parameters: $\rho_1 = 10^3$, $\rho_2 = 10^2$, $\mu_1 = 10$, $\mu_2 = 1$, $\lambda = 24.5$. The dimensionless parameters are then given by: $\mu^\star = \rho^\star = 0.1$, Re $= 35$, Eo $= 10$ and Ca $= 0.286$. The density of the bubble is then ten times smaller than that of the surrounding fluid. The computational domain is $(0, T) \times \Lambda = (0, 3) \times [0, 1] \times [0, 2]$. The bubble, circular at the initial configuration, has the radius $r_0 = 0.25$ and is centered at $\boldsymbol{x} = (0.5, 0.5)$. The no-slip wall conditions are imposed on the top and bottom boundaries, while the free slip conditions $\boldsymbol{u} \cdot \nu = 0$ and $\boldsymbol{t} \cdot \mathbf{D}(\boldsymbol{u}) \cdot \nu = 0$ ($\boldsymbol{t}$ represents any tangent vector on $\partial \Lambda$) are imposed on the right and left boundaries. Let us denote $\boldsymbol{u} = (u_x, u_y)$. We introduce the following benchmark quantities:

$$Y_{\boldsymbol{c}}(t) = \frac{1}{|\Omega(t)|} \int_{\Omega(t)} y(t)\, d\mathbf{x}, \qquad \cancel{c}(t) = \frac{2\sqrt{\pi |\Omega(t)|}}{|\Gamma(t)|} \qquad \text{and} \qquad V_{\boldsymbol{c}}(t) = \frac{1}{|\Omega(t)|} \int_{\Omega(t)} u_y(t)\, d\mathbf{x}.$$

The bubble area $|\Omega|_{\text{exact}} = 0.25^2 \pi$ needs to be preserved along the time evolution. The center of mass is characterized by the y-coordinate $Y_{\boldsymbol{c}}(t)$ and we are particularly interested in the final position $Y_{\boldsymbol{c}}(t = 3)$. The degree of circularity $\cancel{c}(t)$ represents the circumference of a circle having the same area as the bubble. We evaluate the minimum circularity $\cancel{c}_{\min}$ and the corresponding incidence time $t|_{\cancel{c} = \cancel{c}_{\min}}$. The rise velocity $V_{\boldsymbol{c}}(t)$ is computed through its component in the direction opposite to the gravitational vector. Both maximal velocity $V_{\boldsymbol{c},\max}$ and corresponding time incidence $t|_{V_{\boldsymbol{c}} = V_{\boldsymbol{c},\max}}$ are of interest. Let NTS and NEL design the number of time steps and the number of mesh elements, respectively. To study the convergence properties of the method with respect to the reference solution obtained using the finest mesh $q_{\text{t,ref}}$, the error quantifications corresponding to the temporal evolution q_t of the quantity q reads:

$$\|e\|_1 = \frac{\sum\limits_{t=1}^{\text{NTS}} |q_{\text{t,ref}} - q_t|}{\sum\limits_{t=1}^{\text{NTS}} |q_{\text{t,ref}}|}, \qquad \|e\|_2 = \left(\frac{\sum\limits_{t=1}^{\text{NTS}} |q_{\text{t,ref}} - q_t|^2}{\sum\limits_{t=1}^{\text{NTS}} |q_{\text{t,ref}}|^2} \right)^{1/2}, \qquad \|e\|_\infty = \frac{\max\limits_t |q_{\text{t,ref}} - q_t|}{\max\limits_t |q_{\text{t,ref}}|}$$

$$\text{and} \qquad \text{ROC}_i = \frac{\log_{10}\left(\dfrac{\|e^{l-1}\|_i}{\|e^l\|_i} \right)}{\log_{10}\left(\dfrac{h^{l-1}}{h^l} \right)} \qquad \text{with} \qquad i \in \{1, 2, \infty\}.$$

The standard linear interpolation is appropriately applied to the solution q_t, since NTS is smaller than that used for the reference solution. The quantity ROC_i corresponds to the rate of convergence required to indicate how much computational effort is needed to establish a certain accuracy, in which h and l design the mesh size and the mesh refinement level, respectively.
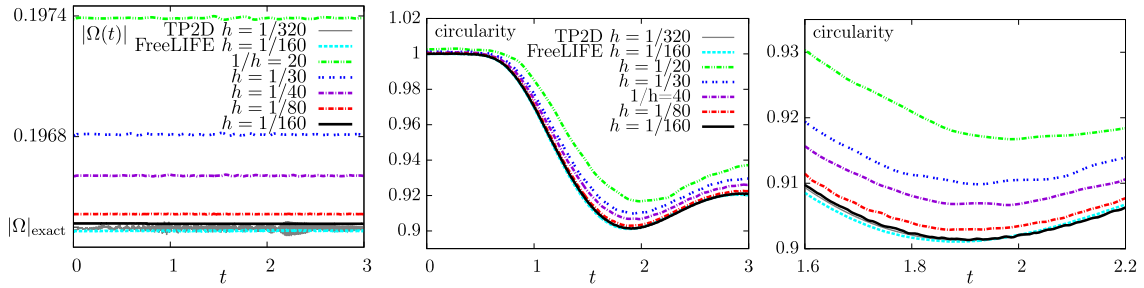
Fig. 3. Temporal evolution of the bubble area (left), the circularity for a complete simulation period (middle) and a close-up of the circularity around the benchmark point $\not{c}_{min}$ (right). Comparisons with reference solutions from Hysing et al. [63]. The same legend is used.
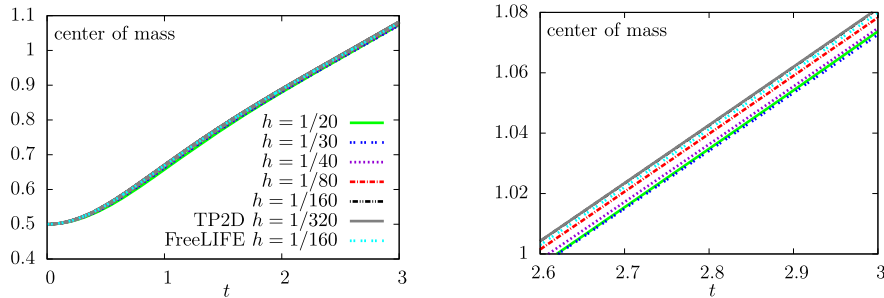

Fig. 4. Temporal evolution of the center of mass and comparison with reference solutions from [63]. (left) Complete simulation period. (right) Close-up around $\boldsymbol{x}_c(t=3)$. The same legend is used.

The computations were performed on non-regular meshes generated using the software Gmsh.[8] The mesh sizes are $1/h \in \left\{20, 30, 40, 80, 100, 160\right\}$ and the corresponding time step sizes are $\Delta t \in \left\{1.77 \times 10^{-2}, 1.77 \times 10^{-2}, 1.42 \times 10^{-2}, 7.12 \times 10^{-3}, 2.83 \times 10^{-3}, 2.22 \times 10^{-3}\right\}$, respectively. The highly accurate reference solution is obtained with the finest mesh size $1/h = 160$ (NEL = 135′110) and NTS = 1′352.

In Fig. 2(left), results of the computed shapes of the ascending bubble, obtained with the finest mesh, are shown at some particular time instants. The shape compactness results from low values of $\mu^\star$ and $\rho^\star$, resulting in high influence of the capillary force on Γ. In Fig. 2(middle), comparisons of the computed interfaces at $T = 3$ with different meshes and with respect to the reference solutions "TP2D" (TU Dortmund – FEM with non-conforming $\tilde{\mathbb{Q}}_1/\mathbb{Q}_0$ basis function for $(\boldsymbol{u}, p)$) and "FreeLIVE" (EPFL Lausanne – FEM with $\mathbb{P}_1 - iso\mathbb{P}_1/\mathbb{P}_1$ elements for $(\boldsymbol{u}, p)$) presented in the benchmark [63]. Results show good agreement between the obtained shapes. We present in Fig. 2(right) a detailed view of the different shapes around the zone of maximal discrepancy. The congruence of our finest result with those obtained by "TP2D" with the finest grid resolution $1/h = 320$ is well seen, while we observe very small differences with the shape obtained by "FreeLIVE" with their finest grid resolution $1/h = 160$.

The temporal evolution of the areas $|\Omega^n|$ with respect to the mesh size are plotted in Fig. 3(left), showing good mass preservation appropriately converging to the exact value $|\Omega|_{exact}$ when $h \to 0$. Fig. 3(middle/right) shows the temporal evolution of the circularity; An overlay with respect to the reference curve obtained by "TP2D" around $\not{c}_{min}$ is achieved. The curves in Fig. 4 showing the temporal evolution of the center of mass Y_c do not reveal significant differences. The close-up view mainly shows the congruence between the curve obtained with the finest mesh and the reference solution "TP2D" in [63]. Fig. 5 shows a good agreement concerning the evolution of the rise velocity with respect to the reference curves. Only an enlarged section around $t|_{V_c = V_{c,max}}$ shows some separation between the curves.

Grid convergence For a quantitative study, we proceed with a comparison with the reference solutions "TP2D", "FreeLIVE" and "MooNMD" in Hysing et al. [63] and with other results from the existing literature Štrubelj et al. [64] (VOF), Klostermann et al. [65] (VOF) and Doyeux et al. [32] (FEM). Table 1 summarizes the benchmark quantities and the results obtained by the previous groups. Our results obtained with $1/h = 160$ serve as a basis in our comparisons. The quantities $\not{c}_{min}$, $t|_{\not{c}=\not{c}_{min}}$, $t|_{V_c=V_{c,max}}$ and $y_c(t=3)$ belongs to the reference range obtained in [63], while $V_{c,max}$ depicts a small difference but is almost equal to the value obtained in [32]. To summarize, this computational study demonstrates good overall agreement with the reference results in [63].

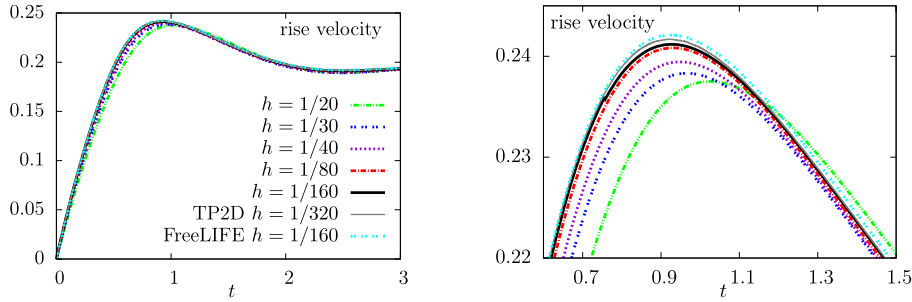---

[8] Gmsh – http://www.geuz.org/gmsh.

Fig. 5. Temporal evolution of the rise velocity and comparison with reference solutions from [63]. (left) Complete simulation period. (right) Close-up around $V_{c,max}$. The same legend is used.

Table 1
Comparisons with benchmark quantities and published results: minimum circularity and maximum rise velocity, with corresponding incidence times, and the final position of the center of mass.

$1/h$	20	40	80	**160**	Benchmark [63]	Štrubelj et al. [64]	Klostermann et al. [65]	Doyeux et al. [32]
ϕ_{min}	0.9167	0.9068	0.9029	**0.90133**	0.9012 ± 0.0001	0.8876	0.9044	0.9001
$t\vert_{\phi=\phi_{min}}$	2.0000	1.8857	1.8714	**1.90507**	1.8895 ± 0.0145	1.8915	1.9625	1.9000
$V_{c,max}$	0.2375	0.2394	0.2408	**0.24119**	0.2419 ± 0.0002	0.2457	0.2348	0.2412
$t\vert_{V_c=V_{c,max}}$	1.0179	0.9428	0.9286	**0.92686**	0.9263 ± 0.005	0.9235	0.9516	0.9248
$y_c(t=3)$	1.0737	1.0748	1.0783	**1.08095**	1.0808 ± 0.0009	1.0679	1.0696	1.0815

Table 2
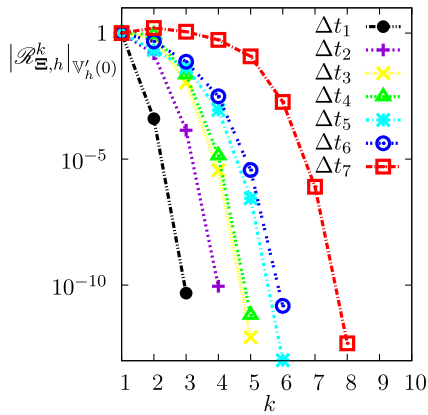Rising bubble benchmark: convergence analysis for some benchmark quantities.

	$1/h$	NTS	NEL	$\Vert e \Vert_1$	ROC$_1$	$\Vert e \Vert_2$	ROC$_2$	$\Vert e \Vert_\infty$	ROC$_\infty$
ϕ	20	169	2064	1.2644E−2		1.4406E−2		2.2068E−2	
	40	211	8538	3.8310E−3	1.72266	4.3667E−3	1.72205	6.2540E−3	1.81910
	80	421	33836	1.0417E−3	1.87878	1.1992E−3	1.86447	1.8479E−3	1.75889
Y_c	20	169	2064	1.5698E−2		1.6304E−2		1.3577E−2	
	40	211	8538	5.9847E−3	1.39123	6.2980E−3	1.37226	5.9427E−3	1.19197
	80	421	33836	2.2548E−3	1.40829	2.5095E−3	1.32749	2.0743E−3	1.51849
V_c	20	169	2064	2.6769E−2		3.9206E−2		7.5292E−2	
	40	211	8538	1.1374E−2	1.23482	1.3310E−2	1.55856	2.3537E−2	1.67757
	80	421	33836	3.5184E−3	1.69275	3.8174E−3	1.80185	6.1753E−3	1.93035
	100	1059	52710	2.3683E−3	1.77392	2.4877E−3	1.91899	3.5091E−3	2.53289

Convergence analysis Finally, we perform a quantitative convergence analysis and we compute both the relative errors and the estimated convergence rates for ϕ, V_c and y_c, as previously defined. Results are depicted in Table 2. The different quantities clearly converge with a more than linear convergence order, approaching 2 for the circularity and the rise velocity. The convergence order for the center of mass is of about 1.5 in both l_1, l_2 and l_∞ norms.

Comparison with respect to the exact Newton method Thereafter, we investigate the convergence properties of the numerical solver and we proceed with a comparison between the inexact Newton strategies (QN1 and QN2) and the exact Newton strategy (N). Using the exact Jacobian matrix, Fig. 6(left) shows the convergence of the residuals for various choices of the time step size Δt. The convergence of the Newton scheme is slower when increasing the time step size, where the starting value of each subiteration becomes far for the expected solution; For large Δt, for instance Δt_7, a plateau is observed for the first iterations and, beyond a critical value of the residual, the convergence becomes subsequently fast. Notice that other techniques can be used to improve the convergence such as the initialization by the solution of the fixed point scheme or the use of the damped-Newton strategy; that is beyond the scope of the present work.
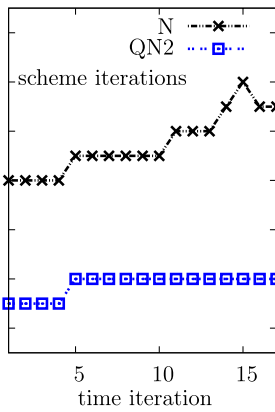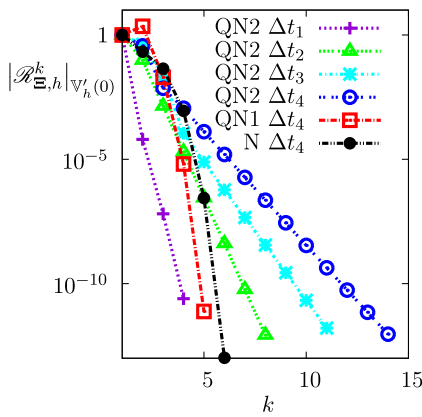
For every time step t^n, we also report the rate of convergence of the Newton algorithm at every subiteration, which is given by the ratio:

$$r(k) = \frac{\ln\left(\frac{\vert \mathscr{R}\left(\Xi_{k,h}^n\right)\vert_{\mathbb{V}_h'(\mathbf{0})}}{\vert \mathscr{R}\left(\Xi_{k-1,h}^n\right)\vert_{\mathbb{V}_h'(\mathbf{0})}}\right)}{\ln\left(\frac{\vert \mathscr{R}\left(\Xi_{k-1,h}^n\right)\vert_{\mathbb{V}_h'(\mathbf{0})}}{\vert \mathscr{R}\left(\Xi_{k-2,h}^n\right)\vert_{\mathbb{V}_h'(\mathbf{0})}}\right)} \quad \text{with} \quad k > 2.$$

Fig. 6. (left) Convergence curves of the exact Newton scheme (N); Results are plotted in the semi-logarithmic scale. (right) Rates of convergence $r(k)$ of the residuals. The time step sizes are $(\Delta t_1, \Delta t_2, \Delta t_3, \Delta t_4, \Delta t_5, \Delta t_6, \Delta t_7) = (0.003, 0.05, 0.08, 0.1, 0.2, 0.3, 0.47)$.

k	Δt_1	Δt_2	Δt_3	Δt_4	Δt_5	Δt_6	Δt_7
1	–	–	–	–	–	–	–
2	–	–	–	–	–	–	–
3	**2.0374**	3.7001	9.6866	24.9240	1.0035	**2.3988**	2.16842
4		2.0388	1.9608	2.0182	2.5004	1.7139	2.03475
5			1.9013	1.9685	2.0657	2.1286	2.76052
6					1.8323	1.8420	1.86335
7							1.84424

Fig. 7. Convergence properties of the inexact Newton strategies (QN1 and QN2) compared versus the convergence of the exact Newton strategy (N). The residuals' convergence curves are plotted in the semi-logarithmic scale. The time step sizes are $(\Delta t_1, \Delta t_2, \Delta t_3, \Delta t_4) = (0.003, 0.01, 0.1, 0.2)$.

Code:	QN2				QN1	N
k	Δt_1	Δt_2	Δt_3	Δt_4	Δt_4	Δt_4
1	–	–	–	–	–	–
2	–	–	–	–	–	–
3	0.7124	1.8201	3.4071	3.8936	5.9081	1.0035
4	**1.1414**	0.9950	1.7566	0.4710	**1.7045**	2.5004
5		1.0045	0.5095	1.1759	**1.6998**	2.0657
6		0.9971	0.9669	0.9710		1.8323
7		1.0018	0.9917	1.0055		
8		0.9951	0.9980	0.9923		
9			0.9999	0.9970		
10			1.0008	0.9941		
11			1.0033	0.9940		
12				0.9944		
13				0.9944		
14				0.9873		

We observe in Fig. 6(right) that $r(k) \approx 2$, which means that a second-order convergence behavior is almost obtained.

We now investigate the convergence speeds for the inexact Newton strategies QN1 and QN2. Fig. 7(left) shows that the second-order convergence of the Newton method is preserved when using the strategy QN1, i.e. by considering the simplifying assumption of signed distance $|\nabla\varphi| = 1$ in Λ, everywhere, since the signed distance property is well established after the redistancing process. However, the quadratic convergence is deteriorated when using the strategy QN2 which disregards the shape derivative terms in the momentum equation (3.5). The convergence rates in Fig. 7(right) clearly show that the quadratic convergence of the exact Newton strategy N is slightly affected when using QN1 but it is remarkably affected when using QN2. In Fig. 7(middle), we report the numbers of the Newton iterations required until reaching the convergence for the time step Δt_3, revealing that the iteration numbers for QN2 is twice to three times larger than that of the exact Newton scheme N. Nevertheless, the strategy QN2 can be somehow useful when using small time steps, since it simplifies the derivatives block assembly in the Jacobian matrix without big changes in the number of iterations.

Comparison with respect to a fully explicit implementation In this paragraph, we provide further insights into the performances of the fully implicit method using the inexact Newton scheme QN1. We perform comparisons with respect to the explicit method commonly used in the literature. We consider the scheme presented in Appendix D in which we consider an explicit implementation of the capillary force and a segregated approach for the coupling with the advection of the interface.

We continue with the setup of the rising bubble aforementioned and computations were performed on a workstation with an Intel® Core™ i7-4790 (3.6 GHz) processor. To investigate the stabilizing capabilities of the implicit method, we perform simulations for several meshes and we report in Table 3 the maximum time step size Δt_{max} allowed by both schemes. Results reveal that the implicit scheme QN1 has a significant stabilizing effect and allows to use larger time steps. In particular, the implicit approach enables to exceed the maximum time step allowed by the explicit scheme by several orders of magnitude, more than sixty times for $h = 1/100$.

We now focus on the computational efforts required by both the implicit and explicit approaches. We perform simulations of the rising bubble in the time interval $(0, 2.5)$ and we measure the wall clock times for serial simulations. The

Table 3
Maximum time step Δt_{max} allowed by the implicit and explicit methods for several values of the mesh size h.

h	Δt_{max} (strategy QN1)	Δt_{max} (explicit method)
1/20	0.73	6.31×10^{-2}
1/40	0.67	3.25×10^{-2}
1/80	0.49	8.37×10^{-3}
1/100	0.35	5.43×10^{-3}

Table 4
Computation time CPU on one processor using the implicit and explicit methods for several values of the mesh size h.

h	CPU (strategy QN1)	CPU (explicit method)
1/40	289	306
1/80	3491	4721
1/100	9667	11850

computing times CPU are reported in Table 4, showing that the implicit approach is computationally cheaper than the explicit approach especially for finer meshes. Thanks to its quadratic convergence, the scheme QN1 allows to use significantly larger time steps and converges usually in less than five iterations. That enables to compensate the computational effort needed for both the assembly of the linear system and the factorization of the Jacobian matrix at each Newton subiteration.

Further improvements of the present methodology based on both the use of mesh adaptation techniques and the development of a cubically convergent Newton variant without evaluating the second-order derivatives are investigated for the capillary problem in a forthcoming work [44].

4.2. Example 2: Dynamics of vesicles under shear flow

In the present example, we proceed with the validation of the proposed methodology and we investigate the dynamics of single vesicle under a linear shear flow. Under such a linear shear flow, the upper and lower boundaries (respectively at y-coordinates L and -L) shall move horizontally with opposite constant velocities $\mathbf{u}_b(\cdot, \pm L) = (\pm V, 0)$, forming consequently the subset Σ_D, see Fig. 1. A free-stress boundary condition $\boldsymbol{\sigma} \boldsymbol{\nu} = \mathbf{0}$ is imposed on Σ_N. The fluid is always initially stationary. In what follows, we adopt an elliptic shape for the two-dimensional cells at the initial position.[9] For a two-dimensional vesicle in a simple shear flow, different regimes of motion patterns have been observed and extensively studied, experimentally [66] theoretically [12] and numerically [67,26,31], in the published literature. Depending on the reduced area χ and the viscosity ratio $\mu^\star$, it is known that two flow regimes may occur. A steady-state tank treading motion, referred to as TT, happens if the viscosity ratio $\mu^\star$ remains small, in which the cell assumes a steady-state ellipsoidal shape such that the equilibrium inclination angle θ remains constant with respect to the flow direction. Beyond a threshold value of the viscosity ratio, the cell starts rotating periodically around its axis, yielding the tumbling regime, referred to as TB. For a fixed reduced area, the transition between the two regimes occurs at a particular value $\mu^\star_{TT/TB}$, resulting in the so called phase diagram. At the computational level, we evaluate the inclination angle $\theta \in [-\pi/2, \pi/2]$ by determining the eigenvectors and the eigenvalues of cell's inertia tensor

$$\boldsymbol{M} = \int_\Omega \left(\boldsymbol{x} - \frac{1}{|\Omega|} \int_\Omega \boldsymbol{x} d\boldsymbol{x} \right) \otimes \left(\boldsymbol{x} - \frac{1}{|\Omega|} \int_\Omega \boldsymbol{x} d\boldsymbol{x} \right) d\boldsymbol{x}$$

around its center of mass (rotational axis). The angle θ represents the angle formed between the eigenvector associated with the largest eigenvalue and the vertical axis in the y-direction.

Let us consider two vesicles having a reduced area $\chi = 0.7$ placed in simple shear flow described by $Ca = 100$ and $Re = 10^{-3}$, where the confinement parameter is $\gamma = 1/2$. The first cell has a viscosity ratio $\mu^\star = 1$. Numerical computations show that the cell undergoes a TT motion where the inclination angle converges to a fixed value $\theta^\star$, see Fig. 8. The computational shapes and the internal fluid flow are also depicted in the snapshots in Fig. 8.

---

[9] Let x and y denote the Cartesian components. For a given reduced area χ, we introduce the following expression for the Eulerian description of a cell forming an inclination angle θ with respect to the horizontal axis:

$$\varphi_0(x, y) = \frac{\sqrt{(x_\theta/\alpha)^2 + y_\theta^2/(2-\alpha^2)}}{\sqrt{(x_\theta/\alpha^2)^2 + y_\theta^2/(2-\alpha^2)^2}} \left(\sqrt{(x_\theta/\alpha)^2 + y_\theta^2/(2-\alpha^2)} - R_0 \right),$$

with $\alpha = \sqrt{1 + \sqrt{1-\chi}}$, $R_0 = 0.45$, $x_\theta = x\cos(\theta) - y\sin(\theta)$ and $y_\theta = x\sin(\theta) + y\cos(\theta)$.

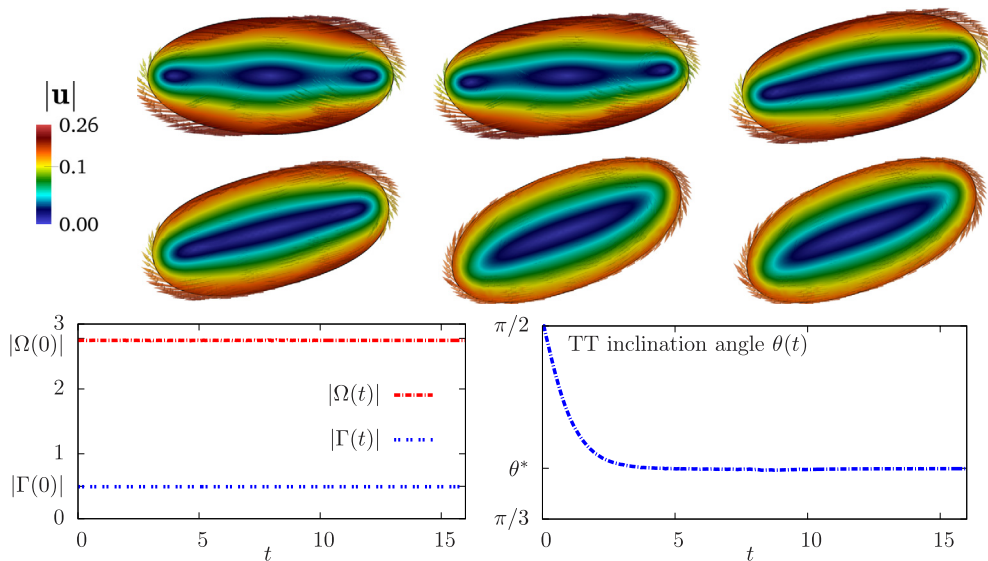**Fig. 8.** Tank treading regime: snapshots showing the dynamic behavior of a cell (shape Γ and velocity profile of the intracellular fluid) with $\chi = 0.7$, $\mu^\star = 1$ and Ca = 100 in a simple shear flow with Re = 10^{-3} and $\gamma = 1/2$ at successive times $t \in \{0, 0.05, 0.15, 0.2, 1, 4\}$, respectively.

The second cell has a viscosity ratio $\mu^\star = 10$, and numerical computations show that the cell undergoes a TB motion where the inclination angle exhibits a periodic regime as depicted in Fig. 9. Snapshots in Fig. 9 show the cell's shapes during one TB period. To check the conservation properties of the outlined numerical method, we follow the evolution of the enclosed area $|\Omega(t)|$ and the membrane length $|\Gamma(t)|$ during the entire simulation for both tank treading and tumbling regimes. Tracings are provided in Fig. 8, and show good conservation properties. Further details about the convergence properties of these both quantities will be provided subsequently in section 4.3.

Effect of the starting angle We now investigate the influence of the starting angle on the dynamics of a vesicle undergoing a TT like motion in the steady state. To that end, let us consider different cells having the same reduced area $\chi = 0.6$ and placed in a linear shear flow characterized by $\mu^\star = 1$, Re = 10^{-3} and Ca = 10^3. The confinement level is $\gamma = 1/2$. The cells, initially ellipsoidal, are started with different inclination angles $\theta(0) \in \{\pi/2, 0, -\pi/4, -\pi/10, -4\pi/10\}$, using the expression of φ_0 previously introduced in this example. The evolution of the cells' inclination angles $\theta(t)$ versus time are plotted in Fig. 10 showing clearly that the different vesicles similarly converge to a TT steady state regime, in which the same angle $\theta^\star$ in obtained. This result is expected since the flow regime should depend on χ and $\mu^\star$, and not on the starting inclination angle or on the geometry of the initial shape. Remark that, for a cell with a starting angle $\theta(0) = -4\pi/10$, a partial tumbling motion is first observed and the cell undergoes the same steady-state TT motion subsequently.

Effect of the confinement level To proceed with the validation of our numerical method, we first explore the effect of the confinement level on the vesicle's regime. To this end, we perform a first numerical simulation of a cell undergoing a TT regime and we explore the influence of the confinement level γ on the equilibrium inclination angle $\theta^\star$. A vesicle having a reduced area $\chi = 0.6$ and a viscosity contrast $\mu^\star = 1$ is placed in a linear shear flow with Ca = 10^3 and Re = 10^{-3}. By varying γ from 1/2 to 1/5, it is revealed that the influence of the confinement is strongly reduced when γ is below 1/4 (see Fig. 11(left)). We now change the viscosity contrast to $\mu^\star = 10$, and the cell switches to a TB regime. We similarly vary γ from 1/2 to 1/5 and compute the TB period as a function of the confinement. Results in Fig. 11(right) show that, below a confinement level $\gamma = 1/4$, the influence of the boundaries starts to be minimized. From now, a confinement parameter $\gamma = 1/4$ will be always considered, unless otherwise stated.

Numerical and experimental validation We thereafter compare our method to some experimental and numerical results known in the published literature. First, we consider vesicles having all a unit viscosity contrast $\mu^\star = 1$ and placed in a linear shear flow characterized by Ca = 10^2 and Re = 10^{-3}. We vary the reduced area $\chi \in [0.6, 1]$ and we determine the corresponding equilibrium inclination angle $\theta^\star$. The different cells adopt the TT regime and we plot $\theta^\star/\pi$ against χ. Computational results are compared to the simulation results of Kraus et al. [69], Zhao et al. [68] and Salac et al. [26]. The results are presented in Fig. 12 showing a good agreement with the results of Salac et al. [26, Fig. 1], while the decay of the equilibrium inclination angle with χ is smaller than the one observed in Kraus et al. [69] and Zhao et al. [68, Fig. 3]. Note that our computational results are also consistent with those obtained recently by Nürnberg and coworkers [15, Fig. 1].

Second, in trying to recreate [68, Fig. 4], we perform similar simulations using different viscosity contrasts $\mu^\star = 2.7$ and $\mu^\star = 5.4$. We particularly focus on the cell's inclination $\theta^\star/\pi$ for larger reduced area $\chi > 0.85$ (almost circular shapes),
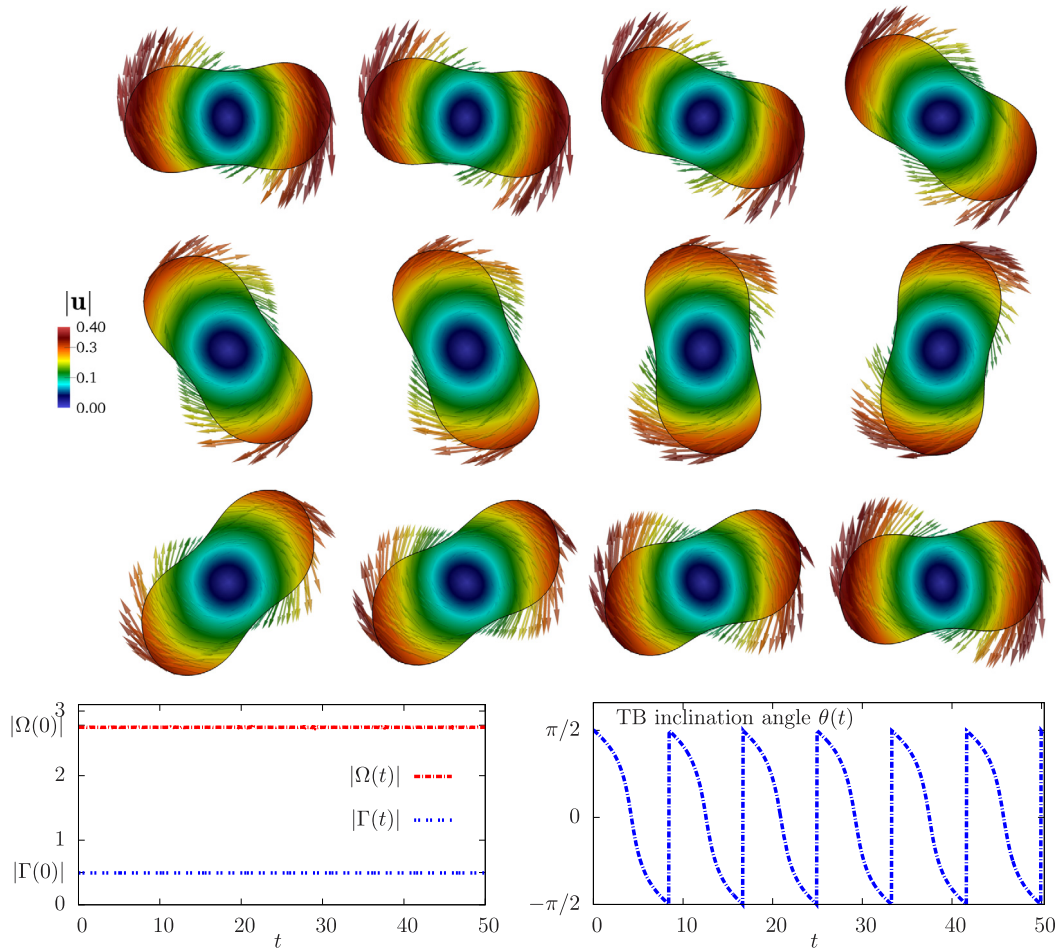
Fig. 9. Tumbling regime: snapshots showing the dynamic behavior of a cell (shape Γ and velocity profile of the intracellular fluid) with $\chi = 0.7$, $\mu^\star = 10$ and Ca $= 100$ in a simple shear flow with Re $= 10^{-3}$ and $\gamma = 1/2$ at successive times $t \in \{26, 27.25, 27.75, 28, 28.5, 29, 29.5, 30.25, 30.5, 30.75, 31.51, 31.5\}$, respectively.
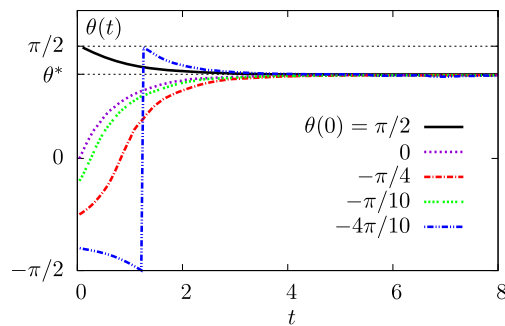

Fig. 10. Influence of the starting inclination angle on the equilibrium inclination angle of a TT cell evolving in a simple shear flow characterized by $\chi = 0.6$, $\mu^\star = 1$, Re $= 10^{-3}$, Ca $= 10^3$ and $\gamma = 1/2$.

and we compare our numerical results with the numerical results obtained by Zhao and Shaqfeh [68, Fig. 3] and the experimental results obtained by Kantsler and Steinberg [66]. Plots are provided in Fig. 12 showing a better agreement compared to the results obtained with a unit viscosity contrast $\mu^\star = 1$.

Moreover, we compare our results with the prediction model of Seifert [8] and the numerical obtained by Salac et al. [26, Fig. 2] and Nürnberg et al. [15, Fig. 2]. To that end, we introduce a second shape parameter, the excess length parameter $\Delta = |\Gamma(0)|\sqrt{2\pi / |\Omega(0)|} - 2\pi$, which represents the shape difference with respect to a circular vesicle ($\Delta = 0$ corresponds to $\chi = 1$). The cell shape can be characterized through the deformation parameter $D = (l - b)/(l + b)$, where l and b represent
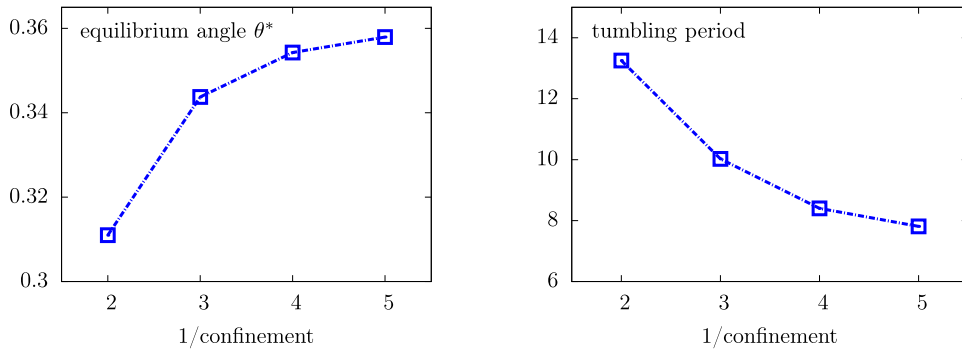
Fig. 11. Left: Influence of the confinement level on the behavior of a TT cell (equilibrium inclination angle) characterized by $\chi = 0.6$ and $\mu^\star = 1$ with Re $= 10^{-3}$ and Ca $= 10^3$. Right: Influence of the confinement level on the behavior of a TB cell (tumbling period) characterized by $\chi = 0.6$ and $\mu^\star = 10$ with Re $= 10^{-3}$ and Ca $= 10^3$.
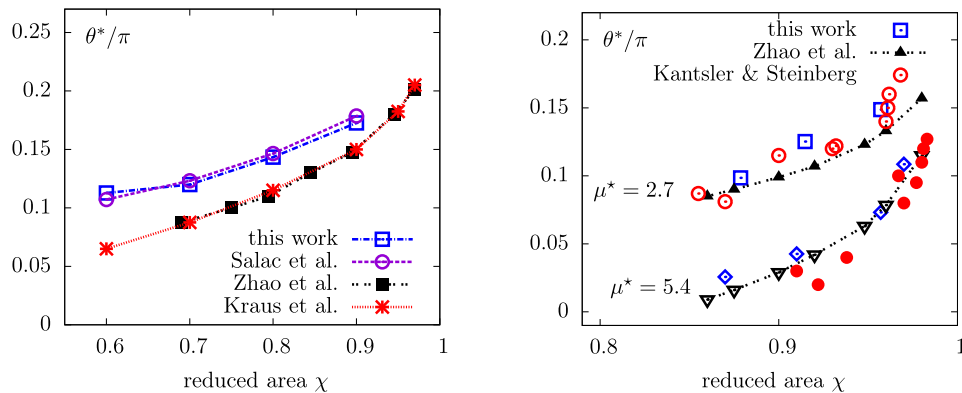

Fig. 12. (left) Equilibrium inclination angle θ^* for vesicles having different reduced area χ and undergoing a TT regime with $\mu^\star = 1$, Re $= 10^{-3}$ and Ca $= 100$. Comparisons are performed with respect to Salac et al. [26] for the same parameters, Zhao et al. [68] (Ca $= 9$) and Kraus et al. [69] (Ca $= 10$). (right) θ^*/π against χ obtained with different viscosity ratios $\mu^\star = 2.7$ and $\mu^\star = 5.4$. Comparisons of our results (blue squares) with the numerical results of Zhao et al. [68] (dotted black lines with triangles) and the experimental results of Kantsler et al. [66] (red circles).
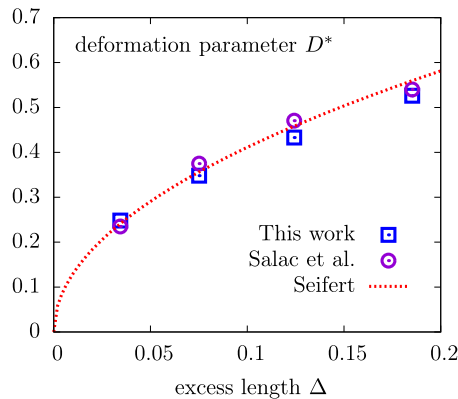

Fig. 13. The deformation parameter $D^\star$ for vesicle in TT regime with respect to the excess length parameter Δ. Comparison with model introduced by Seifert [8] and [26, Fig. 2].

the major and minor semi-axes of an ellipse having the same inertia tensor. For a cell undergoing a TT motion, Seifert [8] introduced a model in which the deformation parameter at equilibrium $D^\star$ scales as $\sqrt{\Delta}$. By varying the excess length parameter Δ, we consider a vesicle in a shear flow characterized by $\mu^\star = 1$, Re $= 10^{-3}$ and Ca $= 100$, and we compute the deformation $D^\star$ at equilibrium against Δ. Results in Fig. 13 show good agreement with the theoretical prediction [8] and the numerical results in [26, Fig. 2].

Finally, we vary the viscosity contrast $\mu^\star$ for a fixed reduced area χ and we focus on the transition line separating the TT regime and the TB regime. In a well-known model introduced by Keller and Skalak [12] where the cell shape was
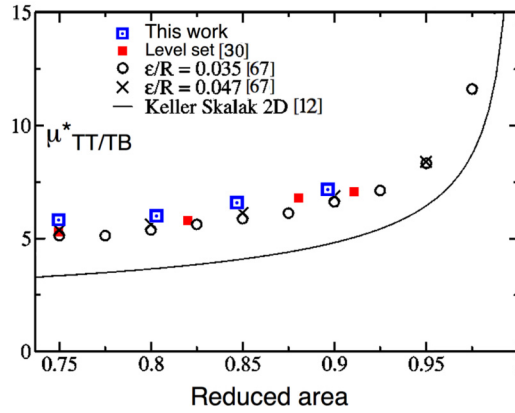
Fig. 14. Phase diagram and comparison with the level set method in [30] (red filled squares), the 2D Keller and Skalac theory [12] and the phase field method [67] (black circles and crosses) where ε denotes the interface width as described in [67].

assumed ellipsoidal throughout the cell dynamics, they report that the transition between the two regimes holds if the viscosity ratio reaches a particular value $\mu^\star_{TT/TB}$ for a fixed χ. Since numerical and analytical studies have been restricted to the Stokes limit [12,67,70], we perform simulations of vesicles under simple shear flow with $Re = 10^{-3}$ and $Ca = 10^3$, and we plot the threshold viscosity contrast $\mu^\star_{TT/TB}$ against χ. Results in Fig. 14 show acceptable agreement with [67] and [30], while we should note that our results are slightly higher. This could be due to the confinement level $\gamma = 1/4$, and we foresee to re-use the anisotropic mesh adaptation procedure described in [24] combined with the outlined method in order to permit the use of much smaller values of γ. Remark that the latter results are larger than those obtained by Salac and coworkers [26, Fig. 3], but they are closer to the results of Nürnberg and coworkers [15, Fig. 3].

Overall, we can conclude that our numerical methodology performs well with respect to the published literature. The use of different boundary conditions and different confinement levels may represent a source of small discrepancies with respect to the other methods.

4.3. Numerical investigation of convergence properties

In this section, we consider vesicles undergoing the tank treading regime at equilibrium and being immersed in the square computational domain in such a way that the confinement parameter is $\gamma = 1/2$. The cell in a simple shear flow is characterized by the reduced areas $\chi \in \{0.6, 0.8\}$, the viscosity ratio $\mu^\star = 2$, the capillary number $Ca = 10^3$ and the Reynolds number $Re = 10^{-3}$. We perform simulations until the TT becomes well established. Analogously to the capillary problem, we proceed herein with a quantitative convergence analysis of our method in the case of the vesicle problem.

Let us consider a highly accurate "reference" solution (referred to by the "bar" symbol) obtained with a mesh size verifying $1/h = 160$ (NEL $= 67'878$) and NTS $= 1'800$. Let $\|\cdot\|_{0,2,\Lambda}$ and $\|\cdot\|_{1,2,\Lambda}$ design the L^2-norm and the H^1 semi-norm, respectively. We first investigate numerically the spatial accuracy of the numerical method by computing normalized errors in the energy norms on successively refined meshes with respect to the refined reference solution. The introduced errors are computed when the TT regime is fully established and are expressed as:

$$E_{\boldsymbol{u}} = \frac{\|\boldsymbol{u}_h - \bar{\boldsymbol{u}}\|_{1,2,\Lambda}}{\|\bar{\boldsymbol{u}}\|_{1,2,\Lambda}}, \ E_p = \frac{\|p_h - \bar{p}\|_{0,2,\Lambda}}{\|\bar{p}\|_{0,2,\Lambda}}, \ E_\lambda = \frac{\|\lambda_h - \bar{\lambda}\|_{0,2,\Gamma}}{\|\bar{\lambda}\|_{0,2,\Gamma}},$$

$$E_\varphi = \frac{\|\mathscr{H}_\varepsilon(\varphi_h) - \mathscr{H}_\varepsilon(\bar{\varphi})\|_{0,2,\Lambda}}{\|\mathscr{H}_\varepsilon(\bar{\varphi})\|_{0,2,\Lambda}} \ \text{and} \ E_\theta = \frac{|\theta^\star_h - \bar{\theta}^\star|}{|\bar{\theta}^\star|}.$$

Table 5 reports the spatial convergence of the computed error in the natural norms, along with the corresponding rates of convergence ROC. The time step sizes are small enough to avoid significantly influencing the accuracy. The number of time steps NTS and the number of mesh elements NEL are also reported in Table 5. By using two different values of the reduced area χ, computations show mainly a suboptimal convergence rates as expected for $E_{\boldsymbol{u}}$, E_p and E_λ. It can be seen that the quantity E_φ converges with more than a linear convergence order, yielding to a convergence order approaching 1.5. The equilibrium inclination angle $\theta^\star$ shows an almost linear convergence behavior.

We additionally observe the evolution of certain quantities for successively refined meshes when the TT regime is established (at time $T \approx 9$). We focus on the following outputs when the mesh size h decreases:

$$q_1 = \|\text{div}\,\boldsymbol{u}\|_{0,2,\Lambda}, \quad q_2 = \|\text{div}_s\,\boldsymbol{u}\|_{0,2,\Gamma}, \quad q_3 = \frac{\big||\Omega(T)| - |\Omega(0)|\big|}{|\Omega(T)|},$$

Table 5
Spatial convergence in the natural norms for vesicles characterized by $\chi = 0.6$ and $\chi = 0.8$ and undergoing a tank-treading motion.

	$1/h$	NTS	NEL	$E_{\boldsymbol{u}}$	ROC$_{\boldsymbol{u}}$	E_p	ROC$_p$	E_λ	ROC$_\lambda$	E_φ	ROC$_\varphi$	E_θ	ROC$_\theta$
	20	180	1060	1.831E−1		3.014E−1		7.409E−1		1.599E−1		2.172E−3	
	30	180	2338	1.582E−1	0.361	2.259E−1	0.711	4.367E−1	1.304	9.974E−2	1.165	1.679E−3	0.634
$\chi = 0.6$	44	180	5190	1.092E−1	0.968	1.818E−1	0.566	2.549E−1	1.404	6.242E−2	1.224	1.164E−3	0.956
	60	360	9482	7.301E−2	1.298	1.257E−1	1.189	1.648E−1	1.407	3.534E−2	1.834	7.951E−4	1.229
	85	900	19210	5.057E−2	1.054	8.686E−2	1.062	1.277E−1	0.733	2.058E−2	1.553	5.966E−4	0.824
$\chi = 0.8$	20	180	1060	2.333E−1		3.291E−1		6.723E−1		4.762E−2		8.753E−3	
	30	180	2338	1.839E−1	0.587	2.558E−1	0.621	4.529E−1	0.974	8.017E−2	1.285	7.298E−3	0.448
	44	180	5190	1.111E−1	1.316	1.514E−1	1.369	2.816E−1	1.240	5.676E−2	0.901	4.639E−3	1.183
	60	360	9482	8.215E−2	0.974	1.073E−1	1.111	1.739E−1	1.555	3.469E−2	1.588	3.072E−3	1.329
	85	900	19210	5.372E−2	1.219	6.927E−2	1.255	1.145E−1	1.199	2.096E−2	1.446	1.909E−3	1.367

Table 6
Convergence history of the quantities q_i, $i = 1, ..., 5$ with respect to the spatial resolution.

	$1/h$	NTS	NEL	q_1	q_2	q_3	q_4	q_5
$\chi = 0.6$	20	180	1060	1.254E−2	1.084E−1	8.451E−4	3.934E−4	5.062E−5
	30	180	1060	9.682E−3	9.853E−2	6.780E−4	4.909E−4	5.248E−6
	44	180	5190	4.878E−3	5.738E−2	4.551E−4	2.533E−4	9.942E−6
	60	900	19210	4.230E−3	4.291E−2	1.269E−5	1.841E−4	3.493E−7
	85	900	19210	2.508E−3	2.910E−2	7.828E−6	5.592E−5	2.598E−7
	160	1800	67878	1.308E−3	1.572E−2	3.932E−6	1.664E−5	7.176E−8
Rate of convergence:				1.058	0.873	1.383	0.884	1.556
$\chi = 0.8$	20	180	1060	2.308E−2	4.438E−1	7.225E−4	9.837E−5	7.036E−6
	30	180	1060	1.077E−2	5.199E−1	6.380E−4	6.608E−5	1.986E−6
	44	180	5190	8.601E−3	2.077E−1	5.5457E−4	1.043E−6	9.212E−7
	60	900	19210	7.965E−3	1.526E−1	2.133E−5	5.207E−5	5.027E−7
	85	900	19210	4.879E−3	9.638E−2	9.913E−6	4.392E−6	3.655E−7
	160	1800	67878	1.986E−3	4.166E−2	4.962E−6	2.132E−6	7.212E−8
Rate of convergence:				1.159	0.951	1.186	0.842	1.491

$$q_4 = \frac{\big|\Gamma(T)\big| - \big|\Gamma(0)\big|}{\big|\Gamma(0)\big|} \quad \text{and} \quad q_5 = \int_\Lambda \big|\boldsymbol{u} \cdot \boldsymbol{n}\big| \, \delta_\varepsilon(\varphi)\big|\nabla\varphi\big|.$$

Convergence history of computed functionals and the corresponding convergence slopes are reported in Table 6, showing clearly an almost first-order accuracy for the computations of q_1, q_2, q_3, q_4 obtained for both $\chi = 0.6$ and $\chi = 0.8$. The quantity q_5 shall approach zero when the TT regime becomes well established. It shows a good convergence behavior of about 1.5.

Similarly to the study performed in Example 4.1, subsection 4.3, we thereafter investigate the convergence of the Newton scheme in the case of the vesicle problem. In particular, we focus on the convergence of the residuals while considering an increasing values of the time step size Δt.

Applying the simplifying assumption $|\nabla\varphi| = 1$ everywhere to the coupled model, we first solve the redistancing problem on a rolling basis (at each time step) and we solve afterwards the variational problem (3.10)–(3.11)–(3.12)–(3.13)–(3.14)–(3.15) obtained with the latter assumption. As tested in Example 4.1, the use of the inexact Jacobian matrix (QN1) under the hypothesis $|\nabla\varphi| = 1$ performs well if the redistancing problem is accurately solved until convergence.

We consider the dynamics of a vesicle having $\chi = 0.6$ in a simple shear flow characterized by Ca $= 10^3$, Re $= 10^{-3}$ and $\mu^\star = 1$. The convergence rate $r(k)$ at each Newton subiteration $k > 1$ is computed as presented in subsection 4.1. The convergence curves and corresponding convergence rates are reported in Fig. 15, showing more than a linear convergence behavior with $1 < r(k) < 2$. The quadratic convergence is deteriorated when increasing gradually Δt. That is expected since the starting values for the Newton loop are not anymore close enough to the expected solutions.

Since the Newton strategy is very sensible to the choice of Δt, we have used an adaptive time step size as described in subsection 3.2.2. During the time interval $[0, 1.1]$, the adapted values of Δt and the corresponding numbers of iterations needed for the Newton convergence are reported in Fig. 16. We observe that usually between 3 and 5 iterations are required to reach the convergence.

Comparison with respect to a fully explicit implementation Similarly to the capillary problem, we perform comparisons between the performances of the present quasi-Newton method, the fully explicit method presented in Appendix D and the fixed point method described in [31, Algorithm 2]. To better show the advantage of using the present fully implicit implementation compared to the fixed point approach developed in [31], we consider a smaller capillary number that those tested in [31], which means considering larger magnitudes of the bending force. The adaptive time scheme is disregarded. Let us consider a vesicle having the reduced areas $\chi = 0.85$ and undergoing the tank treading regime at equilibrium. We
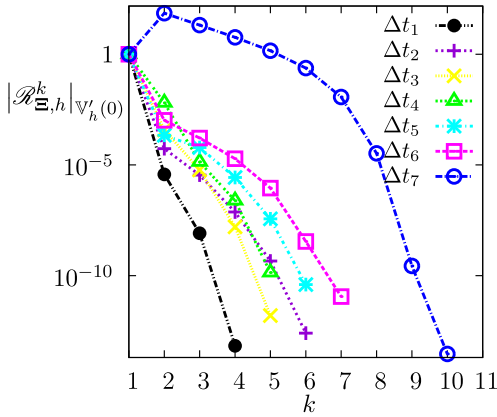
k	Δt_1	Δt_2	Δt_3	Δt_4	Δt_5	Δt_6	Δt_7
1	–	–	–	–	–	–	–
2	–	–	–	–	–	–	–
3	0.4897	0.2799	0.5288	1.2139	0.1508	0.2667	0.2914
4	1.9125	1.3969	1.4203	0.6566	2.4497	1.1745	1.0202
5		1.3295	1.5609	1.8523	1.3817	1.4175	1.0979
6		1.4679			1.5875	1.8161	1.2976
7						1.0305	1.6663
8							1.9449
9							1.9985
10							0.7820

Fig. 15. Convergence properties of the Newton scheme for a vesicle in a simple shear flow. Results are plotted in the semi-logarithmic scale. The time step sizes are $(\Delta t_1, \Delta t_2, \Delta t_3, \Delta t_4, \Delta t_5, \Delta t_6, \Delta t_7) = (0.001, 0.002, 0.003, 0.00487, 0.008, 0.01, 0.03)$.
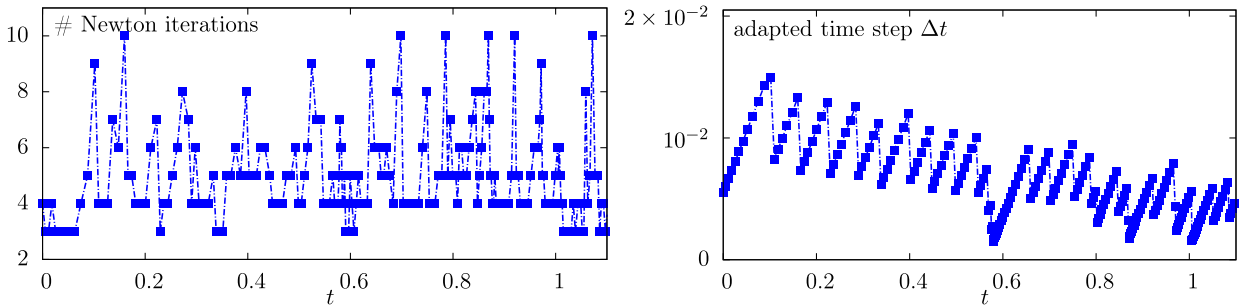

Fig. 16. Vesicle problem. Tracings showing the evolution of number of Newton iterations (Left) and the corresponding adapted time step sizes Δt (Right) for an interval during the simulation.

Table 7
Comparison between the performances of implicit and explicit methods for several mesh sizes. Maximum time step Δt_{max}.

h	Δt_{max} (explicit)	Δt_{max} (fixed point [31])	Δt_{max} (quasi-Newton)
1/20	1.2×10^{-2}	9.1×10^{-2}	0.19
1/44	2.7×10^{-3}	2.1×10^{-2}	7.9×10^{-2}
1/85	6.3×10^{-4}	8.3×10^{-3}	2.5×10^{-2}

set the confinement level $\gamma = 1/2$, the viscosity ratio $\mu^\star = 2.5$, the capillary number $Ca = 10^2$ and the Reynolds number $Re = 10^{-3}$.

We first measure Δt_{max} allowed by the different methods and we report results in Table 7. As expected, the explicit treatment of the highly nonlinear bending force induces a severe time step restriction. Note that further restrictions on Δt should occur if we consider an explicit treatment of the inertia term instead of using the characteristics method. It is important to notice that although fully implicit schemes are in theory unconditionally stable, they cannot completely remove the restrictions on Δt. Indeed, using too large time steps may lead to unphysical results and the numerical errors can cause the divergence of the algorithm. The fixed point method allows using larger time steps than those allowed by the explicit scheme, and stability is maintained for values up to ten times larger. However, the new implicit and monolithic approach proved to be very stable compared to the other methods, and allows to exceed the maximum time step allowed by the explicit implementation of the force by almost forty orders of magnitude.

We perform computations in the time interval $(0, 2)$ and we report the computing times in Table 8. Results clearly show the practical interest of the present method that features significant computational savings with respect to the explicit scheme. That is due mainly to both the quadratic convergence that ensures convergence usually in less than ten iterations, and the banded level set variant that allows to reduce the size of the linear system by assembling locally the equations (3.18)–(3.19)–(3.20). Although the iterative fixed point method enables larger Δt compared to the explicit scheme, it doesn't perform as good as the new method. The large computational cost is mainly due to the iterative resolution of a strongly nonlinear coupling and the linear convergence behavior which is sometimes achieved in more than thirty itera-

Table 8
Comparison between the performances of implicit and explicit methods for several mesh sizes. Simulation timings.

h	CPU (explicit)	CPU (fixed point [31])	CPU (quasi-Newton)
1/20	610	594	518
1/44	3059	2911	2585
1/85	50222	48604	41325

tions. We emphasize that although the present method performs well in 2D, several developments are needed to ensure an affordable computational burden for three-dimensional simulations.

5. Conclusions

We have presented a finite element methodology for the numerical simulation of the dynamics of interfaces and vesicles immersed in a Newtonian fluid. In contrast to the most existing works where the membrane forces are considered with explicit time integration, the present work features the use of a fully implicit and monolithic approach, based on exact and quasi-Newton methods. To the knowledge of the authors, this work presents the first such implicit strategy for the highly nonlinear vesicle problem. That allows to address several stability issues related to the solver when using an explicit decoupling strategy for the membrane force, and especially when the capillary or bending effects dominate. In addition, that enables us to circumvent the high computational burden resulting from the time step limitation, since the time step limitation depends on both the surface tension coefficient/bending rigidity and the mesh size when using fully explicit schemes. Both exact Newton–Raphson and quasi-Newton strategies are investigated and feature a second-order convergence behavior. For the vesicle problem, a banded level set variant allows to handle the singularity of the global matrix of the linear system while featuring, in addition to the parallel implementation, an affordable computational cost. We have reported several numerical simulations obtained with the inexact Newton strategy for the capillary and vesicle problems in the two-dimensional case. We have shown that the mass preservation is achieved at high precision. The convergence studies and comparisons with some benchmark results demonstrate in detail the efficiency and the robustness of the method. Comparisons with experimental measurements and some computational results available in literature show an overall good agreement.

We have developed this method especially for the simulation of single vesicles (more generally for fluidic membranes) in the two-dimensional case. However, the presented work has several limitations common to other numerical approaches that should be progressively improved. We thereafter list some of the straightforward extensions. The extension of the current method to the full three-dimensional case is currently being explored, in which further difficulties related to the full expression of the membrane force arise in the vesicle problem. While the three-dimensional formulation of the surface tension problem does not introduce any changes or additional complexities in the tangent problem, several issues related to the computational cost should be addressed. To that end, we are investigating more sophisticated damped and inexact Newton strategies in order to maintain an affordable computational burden in 3D. We are also focusing on the development of Newton strategies with a third-order convergence and the construction of robust preconditioners that would allow substantial computational savings. We also foresee the use of anisotropic mesh adaptation procedures to improve the computational accuracy in the vicinity of the membrane and in zones of complex flow patterns. Modeling of a dense concentration of RBCs in the full three-dimensional case and studying their interactions in the mesoscopic scale is still too challenging and represents the ultimate goal of our current developments.

Acknowledgements

Appendix A. Useful derivatives and linearization expressions

Let us consider a functional $\mathcal{F}$ that depends on a function $\boldsymbol{x} \to \varphi(\boldsymbol{x})$. Let $D\mathcal{F}[\delta\varphi]$ denote the Gâteaux derivative of $\mathcal{F}(\varphi)$ at φ along the direction $\delta\varphi$. The directional derivatives of some geometrical quantities in the direction of a spatial level set increment $\delta\varphi$ are given by

$$D\nabla\varphi[\delta\varphi] = \nabla\delta\varphi, \quad D|\nabla\varphi|[\delta\varphi] = \nabla\delta\varphi \cdot \boldsymbol{n}, \quad D\frac{1}{|\nabla\varphi|}[\delta\varphi] = \frac{\nabla\delta\varphi \cdot \boldsymbol{n}}{-|\nabla\varphi|^2} \quad \text{and} \quad D\boldsymbol{n}[\delta\varphi] = \frac{\nabla_s\delta\varphi}{|\nabla\varphi|},$$

yielding the following expression for the linearization of the mean curvature in the direction of $\delta\varphi$:

$$DH[\delta\varphi] = D\operatorname{div}_s \boldsymbol{n}[\delta\varphi] = D\operatorname{div}\boldsymbol{n}[\delta\varphi] - (D\nabla\boldsymbol{n}[\delta\varphi]\boldsymbol{n}) \cdot \boldsymbol{n} - \nabla\boldsymbol{n} : (D\boldsymbol{n}[\delta\varphi] \otimes \boldsymbol{n} + \boldsymbol{n} \otimes D\boldsymbol{n}[\delta\varphi]).$$

Since we have $\boldsymbol{n} \cdot \nabla_s\delta\varphi = 0$, the equation $\nabla\nabla_s\delta\varphi : \boldsymbol{n} \otimes \boldsymbol{n} + \nabla\boldsymbol{n} : \nabla_s\delta\varphi \otimes \boldsymbol{n} = 0$ holds and leads to

$$DH[\delta\varphi] = \mathrm{div}\left(\frac{\nabla_s\delta\varphi}{|\nabla\varphi|}\right).$$

Since $\nabla\varphi$ is curl-free, we easily show that:

$$\boldsymbol{n}\cdot\nabla\nabla\varphi = \nabla|\nabla\varphi| \qquad \text{and} \qquad \boldsymbol{n}\cdot\nabla\boldsymbol{n} = \frac{1}{|\nabla\varphi|}\big((\mathbf{Id}-\boldsymbol{n}\otimes\boldsymbol{n})\nabla\nabla\varphi\big)\boldsymbol{n} = \frac{\nabla_s|\nabla\varphi|}{|\nabla\varphi|}.$$

Using the Einstein sum rule for repeated indices, the Gauss curvature shall verify:

$$2K = H^2 - \nabla_s\boldsymbol{n} : \nabla_s\boldsymbol{n}^T = H^2 - |\nabla_s\boldsymbol{n}|^2 = \mathrm{div}\left(\frac{H\nabla\varphi - \nabla_s|\nabla\varphi|}{|\nabla\varphi|}\right),$$

yielding to $H(H^2-4K) = 2H\,\mathrm{div}\left(|\nabla\varphi|^{-1}\nabla_s|\nabla\varphi|\right) - \mathrm{div}\left(H^2\boldsymbol{n}\right)$. The directional derivative of the Gauss curvature reads:

$$DK[\delta\varphi] = H\,\mathrm{div}\,\frac{\nabla_s\delta\varphi}{|\nabla\varphi|} - \nabla\boldsymbol{n}:\nabla\left(\frac{\nabla_s\delta\varphi}{|\nabla\varphi|}\right).$$

The directional derivatives of the regularized viscosity and density read:

$$D\mu_\varepsilon(\varphi)[\delta\varphi] = (1-\mu^\star)\delta_\varepsilon(\varphi)\delta\varphi \qquad \text{and} \qquad D\rho_\varepsilon(\varphi)[\delta\varphi] = (1-\rho^\star)\delta_\varepsilon(\varphi)\delta\varphi.$$

Appendix B. Full tangent system of the vesicle problem

The full tangent system associated to the vesicle problem $\mathscr{P}^n$ (3.1), (3.2), (3.3), (3.4) reads:

Given Ξ^k, *find* $\delta\Xi^k \equiv \left(\delta\boldsymbol{u}^k, \delta p^k, \delta\lambda^k, \delta\Phi^k, \delta\Psi^k, \delta\varphi^k\right) \in \mathbb{V}(\boldsymbol{u}_b)\times\mathbb{Q}\times\mathbb{Q}\times\mathbb{X}\times\mathbb{X}\times\mathbb{X}(\varphi_b)$ *such that*

$$
\begin{aligned}
&\mathrm{Re}\,m\left(\delta\boldsymbol{u}^k,\boldsymbol{v};\frac{3\rho_\varepsilon(\varphi^k)}{2\Delta t}\right) + \mathrm{Re}\,c\left(\delta\boldsymbol{u}^k,\boldsymbol{v};\rho_\varepsilon(\varphi^k),\boldsymbol{u}^k\right) + a\left(\delta\boldsymbol{u}^k,\boldsymbol{v};\mu_\varepsilon\left(\varphi^k\right)\right) + (1-\mu^\star)h\left(\delta\varphi^k,\boldsymbol{v};\delta_\varepsilon\left(\varphi^k\right),\boldsymbol{u}^k\right) \\
&\quad + b\left(\boldsymbol{v},\delta p^k;\mathbf{Id}\right) + b\left(\boldsymbol{v},\delta\lambda^k;|\nabla\varphi^k|\delta_\varepsilon\left(\varphi^k\right)\left(\mathbf{Id}-\boldsymbol{n}^k\otimes\boldsymbol{n}^k\right)\right) + b\left(\boldsymbol{v},\delta\varphi^k;|\nabla\varphi^k|\lambda^k\delta'_\varepsilon\left(\varphi^k\right)\left(\mathbf{Id}-\boldsymbol{n}^k\otimes\boldsymbol{n}^k\right)\right) \\
&\quad - k\left(\delta\varphi^k,\boldsymbol{v};\lambda^k\delta_\varepsilon\left(\varphi^k\right)\boldsymbol{n}^k,\left(\mathbf{Id}-\boldsymbol{n}^k\otimes\boldsymbol{n}^k\right)\right) + l\left(\delta\varphi^k,\boldsymbol{v};\lambda^k\delta_\varepsilon\left(\varphi^k\right)\boldsymbol{n}^k,\left(\mathbf{Id}-\boldsymbol{n}^k\otimes\boldsymbol{n}^k\right)\right) \\
&\quad - \frac{1}{\mathrm{Ca}}g\left(\delta\Phi^k,\boldsymbol{v};\delta_\varepsilon\left(\varphi^k\right)\nabla\varphi^k\right) \\
&\quad + \mathrm{Re}(1-\rho^\star)g\left(\delta\varphi^k,\boldsymbol{v};\delta_\varepsilon\left(\varphi^k\right)\left(\frac{3\boldsymbol{u}^k-4\boldsymbol{u}^{n-1}+\boldsymbol{u}^{n-2}}{2\Delta t}+\boldsymbol{u}^k\cdot\nabla\boldsymbol{u}^k\right)\right) \\
&\quad - \frac{1}{2\mathrm{Ca}}g\left(\delta\varphi^k,\boldsymbol{v};\left(2\Phi^k+\left(\Psi^k\right)^3\right)\delta'_\varepsilon\left(\varphi^k\right)\nabla\varphi^k\right) \\
&\quad - \frac{3}{2\mathrm{Ca}}g\left(\delta\Psi^k,\boldsymbol{v};\left(\Psi^k\right)^2\delta_\varepsilon\left(\varphi^k\right)\nabla\varphi^k\right) - \frac{1}{2\mathrm{Ca}}d\left(\delta\varphi^k,\boldsymbol{v};\left(2\Phi^k+\left(\Psi^k\right)^3\right)\delta_\varepsilon\left(\varphi^k\right)\right) \\
&\quad = -\left\langle\mathscr{R}_\Xi\left(\Xi^{T,k}\right),\boldsymbol{v}\right\rangle_{\mathbb{V}(\mathbf{0})',\mathbb{V}(\mathbf{0})}, \\[4pt]
&b\left(\delta\boldsymbol{u}^k,q;\mathbf{Id}\right) = -\left\langle\mathscr{R}_p\left(\boldsymbol{u}^k\right),q\right\rangle_{\mathbb{Q}',\mathbb{Q}}, \\[4pt]
&i\left(\delta\varphi^k,\eta;-\delta_\varepsilon\left(\varphi^k\right)\left(\left(\mathbf{Id}-\boldsymbol{n}^k\otimes\boldsymbol{n}^k\right):\nabla\boldsymbol{u}^k\right)\boldsymbol{n}^k\right) - e\left(\delta\varphi^k,\eta;\delta'_\varepsilon\left(\varphi^k\right)\left(\mathbf{Id}-\boldsymbol{n}^k\otimes\boldsymbol{n}^k\right):\nabla\boldsymbol{u}^k|\nabla\varphi^k|\right) \\
&\quad + b\left(\delta\boldsymbol{u}^k,\eta;|\nabla\varphi^k|\delta_\varepsilon\left(\varphi^k\right)\left(\mathbf{Id}-\boldsymbol{n}^k\otimes\boldsymbol{n}^k\right)\right) + j\left(\delta\varphi^k,\eta;\boldsymbol{u}^k,\delta_\varepsilon\left(\varphi^k\right)\boldsymbol{n}^k,\left(\mathbf{Id}-\boldsymbol{n}^k\otimes\boldsymbol{n}^k\right)\right) \\
&\quad = -\left\langle\mathscr{R}_\lambda\left(\boldsymbol{u}^k\right),\eta\right\rangle_{\mathbb{W}',\mathbb{W}}, \\[4pt]
&n\left(\delta\varphi^k,\phi;\boldsymbol{n}^k,\left(\mathbf{Id}-\boldsymbol{n}^k\otimes\boldsymbol{n}^k\right)\nabla\Psi^k\right) + i\left(\delta\varphi^k,\phi;\Phi^k\boldsymbol{n}^k\right) + f\left(\delta\Psi^k,\phi;|\nabla\varphi^k|\left(\mathbf{Id}-\boldsymbol{n}^k\otimes\boldsymbol{n}^k\right)\right) + e\left(\delta\Phi^k,\phi;|\nabla\varphi^k|\right) \\
&\quad - n\left(\delta\varphi^k,\phi;\left(\mathbf{Id}-\boldsymbol{n}^k\otimes\boldsymbol{n}^k\right)\nabla\Psi^k,\boldsymbol{n}^k\right) - f\left(\delta\varphi^k,\phi;\left(\boldsymbol{n}^k\cdot\nabla\Psi^k\right)\left(\mathbf{Id}-\boldsymbol{n}^k\otimes\boldsymbol{n}^k\right)\right) = -\left\langle\mathscr{R}_\Phi\left(\Phi^k,\Psi^k,\varphi^k\right),\phi\right\rangle_{\mathbb{X}',\mathbb{X}},
\end{aligned}
$$

$$e\left(\delta\Psi^k,\xi;1\right)+f\left(\delta\varphi^k,\xi;\frac{1}{|\nabla\varphi^k|}\left(\mathbf{Id}-\boldsymbol{n}^k\otimes\boldsymbol{n}^k\right)\right)=-\langle\mathscr{R}_\Psi\left(\Psi^k,\varphi^k\right),\xi\rangle_{\mathbb{X}',\mathbb{X}},$$

$$e\left(\delta\varphi^k,\psi;\frac{3}{2\Delta t}\right)+i\left(\delta\varphi^k,\psi;\boldsymbol{u}^k\right)+g\left(\psi,\delta\boldsymbol{u}^k;\nabla\varphi^k\right)=-\langle\mathscr{R}_\varphi\left(\varphi^k,\boldsymbol{u}^k\right),\psi\rangle_{\mathbb{X}(0)',\mathbb{X}(0)},$$

for all $(\boldsymbol{v},q,\eta,\phi,\xi,\psi)\in\mathbb{V}(\mathbf{0})\times\mathbb{Q}\times\mathbb{Q}\times\mathbb{X}\times\mathbb{X}\times\mathbb{X}(0)$, where the corresponding residuals are given by:

$$\left\langle\mathscr{R}_\Xi\left(\Xi^{T,k}\right),\boldsymbol{v}\right\rangle_{\mathbb{V}(\mathbf{0})',\mathbb{V}(\mathbf{0})}=\operatorname{Re}m\left(\frac{3\boldsymbol{u}^k-4\boldsymbol{u}^{n-1}+\boldsymbol{u}^{n-2}}{2\Delta t},\boldsymbol{v};\rho_\varepsilon\left(\varphi^k\right)\right)+\frac{\operatorname{Re}}{2}c\left(\boldsymbol{u}^k,\boldsymbol{v};\rho_\varepsilon\left(\varphi^k\right),\boldsymbol{u}^k\right)$$

$$+a\left(\boldsymbol{u}^k,\boldsymbol{v};\mu_\varepsilon\left(\varphi^k\right)\right)+b\left(\boldsymbol{v},p^k;\mathbf{Id}\right)+b\left(\boldsymbol{v},\lambda^k;|\nabla\varphi^k|\delta_\varepsilon\left(\varphi^k\right)\left(\mathbf{Id}-\boldsymbol{n}^k\otimes\boldsymbol{n}^k\right)\right)$$

$$-\frac{1}{2\mathrm{Ca}}d\left(\varphi^k,\boldsymbol{v};\left(2\Phi^k+(\Psi^k)^3\right)\delta_\varepsilon\left(\varphi^k\right)\right),$$

$$\left\langle\mathscr{R}_p\left(\boldsymbol{u}^k\right),q\right\rangle_{\mathbb{Q}',\mathbb{Q}}=b\left(\boldsymbol{u}^k,q;\mathbf{Id}\right),$$

$$\left\langle\mathscr{R}_\lambda\left(\boldsymbol{u}^k\right),\eta\right\rangle_{\mathbb{Q}',\mathbb{Q}}=b\left(\boldsymbol{u}^k,\eta;|\nabla\varphi^k|\delta_\varepsilon\left(\varphi^k\right)\left(\mathbf{Id}-\boldsymbol{n}^k\otimes\boldsymbol{n}^k\right)\right),$$

$$\left\langle\mathscr{R}_\Phi\left(\Phi^k,\Psi^k,\varphi^k\right),\phi\right\rangle_{\mathbb{X}',\mathbb{X}}=e\left(\Phi^k,\phi;|\nabla\varphi^k|\right)+f\left(\Psi^k,\phi;|\nabla\varphi^k|\left(\mathbf{Id}-\boldsymbol{n}^k\otimes\boldsymbol{n}^k\right)\right),$$

$$\left\langle\mathscr{R}_\varphi\left(\varphi^k,\boldsymbol{u}^k\right),\psi\right\rangle_{\mathbb{X}(0)',\mathbb{X}(0)}=e\left(\frac{3\varphi^k-4\varphi^{n-1}+\varphi^{n-2}}{2\Delta t}-\varsigma^n,\psi;1\right)+d\left(\varphi^k,\boldsymbol{u}^k;\psi\right),$$

$$\left\langle\mathscr{R}_\Psi\left(\Psi^k,\varphi^k\right),\xi\right\rangle_{\mathbb{X}',\mathbb{X}}=e\left(\Psi^k,\xi;1\right)+f\left(\varphi^k,\xi;|\nabla\varphi^k|^{-1}\mathbf{Id}\right).$$

Appendix C. Alternative variational formulation with the mass lumping technique

To reduce the size of the global matrix of the linear system (3.16)–(3.17)–(3.18)–(3.19)–(3.20)–(3.21), we can eliminate the variables $\delta\Phi^n_{k,h}$ and $\delta\Psi^n_{k,h}$ by inverting the operator associated to the corresponding bilinear forms. By using a discontinuous finite element approximation, the corresponding mass matrix is block-diagonal and it can be fully inverted at the element level. We rather consider the following finite dimensional space for $\delta\Psi^n_{k,h}$ and $\delta\Phi^n_{k,h}$:

$$\mathbb{Y}_h=\left\{\varphi\in L^2\left(\overline{\Lambda}\right),\varphi_{|K}\in\mathbb{P}^2_1(K),\forall K\in\mathscr{T}_h\right\}.$$

Since $\mathcal{J}^{-1}$ exists, we have

$$\left\langle\delta\Psi^n_{k,h},\xi_h\right\rangle=-\left\langle\mathcal{J}^{-1}\left(\mathcal{K}\left(\delta\varphi^n_{k,h}\right)\right)+\mathcal{J}^{-1}\left(\mathscr{R}_\Psi\right),\xi_h\right\rangle,\qquad\forall\xi_h.$$

Therefore, the corresponding term in (3.16) reads

$$\left\langle\mathcal{F}\left(\delta\Psi^n_{k,h}\right),\boldsymbol{v}_h\right\rangle=-\left\langle\mathcal{F}\left(\mathcal{J}^{-1}\left(\mathcal{K}\left(\delta\varphi^n_{k,h}\right)\right)\right),\boldsymbol{v}_h\right\rangle-\left\langle\mathcal{F}\left(\mathcal{J}^{-1}\left(\mathscr{R}_\Psi\right)\right),\boldsymbol{v}_h\right\rangle,\qquad\forall\boldsymbol{v}_h.$$

Analogously, we perform for $\delta\Phi^n_{k,h}$ in (3.19) and $\mathcal{E}$ in (3.16), which leads to the reduced final system.

Appendix D. Explicit implementation of the membrane forces

The surface tension problem   To compare the performances of the fully implicit methodology (inexact Newton variant QN1) to the explicit method, we consider an explicit treatment of the capillary force in the momentum equation. The Navier–Stokes equations and the level set equation are solved in a segregated manner. We first advect the level set function using the velocity computed at the previous time step. The capillary force is subsequently computed and added as a source term in the right hand side of the momentum equation. Finally, we solve the Navier–Stokes problem using a monolithic approach.

Regarding the approximation of the inertia term in the momentum equation, we employ a second-order characteristics method. Let $\mathcal{X}(\cdot,\boldsymbol{x},t)$ represent the characteristic curve passing through $\boldsymbol{x}\in\Lambda$ at time t. Let $\boldsymbol{u}^\star=2\boldsymbol{u}^{n-1}-\boldsymbol{u}^{n-2}$ be a prediction by second-order extrapolation of $\boldsymbol{u}$ at t^n. The first-order characteristics is given by $\mathcal{X}^{n-1}_{(1)}(\boldsymbol{x})=\boldsymbol{x}-\Delta t\,\tilde{\boldsymbol{u}}(\boldsymbol{x})$ for all $\boldsymbol{x}\in\Lambda$, while the second-order characteristics is given by $\mathcal{X}^{n-2}_{(2)}(\boldsymbol{x})=\boldsymbol{x}-2\Delta t\,\tilde{\boldsymbol{u}}(\boldsymbol{x})$. The overall explicit scheme is detailed as follows:

1. Compute φ^n such that

$$3\varphi^n = 4\varphi^{n-1} o\mathcal{X}_{(1)}^{n-1} - \varphi^{n-2} o\mathcal{X}_{(2)}^{n-2}.$$

2. Compute the capillary force $\boldsymbol{F}_\Gamma^n$ using (2.1).
3. Compute $\boldsymbol{u}^n$ and p^n such that

$$\frac{\mathrm{Re}}{2\Delta t}\rho_\varepsilon\left(\varphi^n\right)\left(3\boldsymbol{u}^n - 4\boldsymbol{u}^{n-1}o\mathcal{X}_{(1)}^{n-1} + \boldsymbol{u}^{n-2}o\mathcal{X}_{(2)}^{n-2}\right) - \mathbf{div}\left(2\mu_\varepsilon\left(\varphi^n\right)\mathbf{D}\left(\boldsymbol{u}^n\right)\right) + \nabla p^n$$
$$= \boldsymbol{F}_\Gamma^n\left|\nabla\varphi^n\right|\delta_\varepsilon\left(\varphi^n\right) + \mathrm{Re}\,\rho_\varepsilon\left(\varphi^n\right)\boldsymbol{g}, \quad \text{in } \Lambda$$
$$\mathrm{div}\,\boldsymbol{u}^n = 0, \qquad \text{in } \Lambda.$$

The vesicle problem Analogously, we consider an explicit treatment of the bending force in the vesicle problem. The membrane is advected prior to the computation of the flow velocity and pressure (in a segregated manner). After advecting the level set function φ, the mean curvature H and the normal vector $\boldsymbol{n}$ are computed and projected in the appropriate finite element spaces. Based on a duality argument, the surface divergence of H is computed as detailed in [31, Section 3.2.2]. Therefore, the bending force $\boldsymbol{F}_\Gamma$ appears as an explicit source term in the momentum equation. Finally, the fluid problem is solved iteratively using the preconditioned conjugate gradient algorithm, as implemented in [57, Chap. 6]. The explicit decoupling scheme can be summarized as follows:

1. Compute φ^n such that

$$3\varphi^n = 4\varphi^{n-1} o\mathcal{X}_{(1)}^{n-1} - \varphi^{n-2} o\mathcal{X}_{(2)}^{n-2}.$$

2. Compute the bending force $\boldsymbol{F}_\Gamma^n$ (2.3).
3. Compute iteratively $\boldsymbol{u}^n$, p^n and λ^n such that

$$\mathrm{Re}\,\rho_\varepsilon(\varphi^n)\left(\frac{3\boldsymbol{u}^n - 4\boldsymbol{u}^{n-1}o\mathcal{X}_{(1)}^{n-1} + \boldsymbol{u}^{n-2}o\mathcal{X}_{(2)}^{n-2}}{2\Delta t}\right) - \mathbf{div}\left(2\mu(\varphi^n)\mathbf{D}\left(\boldsymbol{u}^n\right)\right) + \nabla p^n = \boldsymbol{0}, \qquad \text{in } \Lambda$$
$$\mathrm{div}\,\boldsymbol{u}^n = 0, \qquad \text{in } \Lambda$$
$$\mathrm{div}_s^n\,\boldsymbol{u}^n = 0, \qquad \text{on } \Gamma^n$$
$$\left[\boldsymbol{\sigma}^n\boldsymbol{n}^n\right]_-^+ = \nabla_s^n\lambda^n - \lambda^n H^n\boldsymbol{n}^n + \boldsymbol{F}_\Gamma^n, \qquad \text{on } \Gamma^n.$$

References

[1] J.U. Brackbill, D.B. Kothe, C. Zemach, A continuum method for modeling surface tension, J. Comput. Phys. 100 (2) (1992) 335–354, http://dx.doi.org/10.1016/0021-9991(92)90240-Y.
[2] J.W. Barrett, H. Garcke, R. Nürnberg, Stable finite element approximations of two-phase flow with soluble surfactant, J. Comput. Phys. 297 (C) (2015) 530–564, http://dx.doi.org/10.1016/j.jcp.2015.05.029.
[3] W.J. Rider, D.B. Kothe, Reconstructing volume tracking, J. Comput. Phys. 141 (2) (1998) 112–152, http://dx.doi.org/10.1006/jcph.1998.5906.
[4] R. Scardovelli, S. Zaleski, Direct numerical simulation of free-surface and interfacial flow, Annu. Rev. Fluid Mech. 31 (1) (1999) 567–603, http://dx.doi.org/10.1146/annurev.fluid.31.1.567.
[5] J.A. Sethian, P. Smereka, Level set methods for fluid interfaces, Annu. Rev. Fluid Mech. 35 (1) (2003) 341–372, http://dx.doi.org/10.1146/annurev.fluid.35.101101.161105.
[6] S. Gross, A. Reusken, Numerical Methods for Two-Phase Incompressible Flows, vol. 40, Springer, Berlin, Heidelberg, 2011.
[7] S.L. Anna, Droplets and bubbles in microfluidic devices, Annu. Rev. Fluid Mech. 48 (1) (2016) 285–309, http://dx.doi.org/10.1146/annurev-fluid-122414-034425.
[8] U. Seifert, Configurations of fluid membranes and vesicles, Adv. Phys. 46 (1997) 13–137, http://dx.doi.org/10.1080/00018739700101488.
[9] P.M. Vlahovska, T. Podgorski, C. Misbah, Vesicles and red blood cells in flow: from individual dynamics to rheology, C. R. Phys. 10 (2009) 775–789, http://dx.doi.org/10.1016/j.crhy.2009.10.001.
[10] H. Song, Y. Hashash, Characterization of stress–strain behaviour of red blood cells (RBCs), part II: response of malaria-infected RBCs, Inverse Probl. Sci. Eng. 23 (3) (2015) 413–424, http://dx.doi.org/10.1080/17415977.2014.922072.
[11] S.A. Safran, Statistical Thermodynamics of Surfaces, Interfaces and Membranes, Frontier in Physics, vol. 90, Addison–Wesley Publishing Company, Reading, Massachusetts, 1994.
[12] S.R. Keller, R. Skalak, Motion of a tank-treading ellipsoidal particle in a shear flow, J. Fluid Mech. 120 (1982) 27–47, http://dx.doi.org/10.1017/S0022112082002651.
[13] W. Choi, J. Yi, Y. Kim, Fluctuations of red blood cell membranes: the role of the cytoskeleton, Phys. Rev. E 92 (2015) 012717, http://dx.doi.org/10.1103/PhysRevE.92.012717.
[14] G. Dziuk, Computational parametric Willmore flow, Numer. Math. 111 (1) (2008) 55–80, http://dx.doi.org/10.1007/s00211-008-0179-1.
[15] J.W. Barrett, H. Garcke, R. Nürnberg, Numerical computations of the dynamics of fluidic membranes and vesicles, Phys. Rev. E 92 (2015) 052704, http://dx.doi.org/10.1103/PhysRevE.92.052704.
[16] P. Canham, The minimum energy of bending as a possible explanation of the biconcave shape of the human red blood cell, J. Theor. Biol. 26 (1970) 61–81, http://dx.doi.org/10.1016/S0006-3495(73)86044-8.
[17] W. Helfrich, Elastic properties of lipid bilayers: theory and possible experiments, Z. Naturforsch. Teil C 28 (1973) 693–703, http://dx.doi.org/10.1515/znc-1973-11-1209.

A. Laadhari et al. / Journal of Computational Physics 343 (2017) 271–299

[18] H. Deuling, W. Helfrich, The curvature elasticity of fluid membranes: a catalog of vesicle shapes, J. Phys. (Paris) 37 (1976) 1335–1345, http://dx.doi.org/10.1051/jphys:0197600370110133500.

[19] E.A. Evans, Bending resistance and chemically induced moments in membrane bilayers, Biophys. J. 14 (12) (1974) 923–931, http://dx.doi.org/10.1016/S0006-3495(74)85959-X.

[20] A. Laadhari, C. Misbah, P. Saramito, On the equilibrium equation for a generalized biological membrane energy by using a shape optimization approach, Physica D 239 (2010) 1567–1572, http://dx.doi.org/10.1016/j.physd.2010.04.001.

[21] T.K.-K. Au, T.Y.-H. Wan, Analysis on an ODE arisen from studying the shape of a red blood cell, J. Math. Anal. Appl. 282 (1) (2003) 279–295, http://dx.doi.org/10.1016/s0022-247x(03)00148-3.

[22] Q. Du, C. Liu, X. Wang, Simulating the deformation of vesicle membranes under elastic bending energy in three dimension, J. Comput. Phys. 212 (2006) 757–777, http://dx.doi.org/10.1016/j.jcp.2005.07.020.

[23] F. Feng, W.S. Klug, Finite element modeling of lipid bilayer membranes, J. Comput. Phys. 220 (1) (2006) 394–408, http://dx.doi.org/10.1016/j.jcp.2006.05.023.

[24] A. Laadhari, P. Saramito, C. Misbah, An adaptive finite element method for the modeling of the equilibrium of red blood cells, Int. J. Numer. Methods Fluids 80 (7) (2016) 397–428, http://dx.doi.org/10.1002/fld.4086.

[25] D. Salac, M. Miksis, A level set projection model of lipid vesicles in general flows, J. Comput. Phys. 230 (22) (2011) 8192–8215, http://dx.doi.org/10.1016/j.jcp.2011.07.019.

[26] D. Salac, M. Miksis, Reynolds number effects on lipid vesicles, J. Fluid Mech. 711 (2012) 122–146, http://dx.doi.org/10.1017/jfm.2012.380.

[27] Q. Du, C. Liu, X. Wang, A phase field approach in the numerical study of the elastic bending energy for vesicle membranes, J. Comput. Phys. 198 (2004) 450–468, http://dx.doi.org/10.1016/j.jcp.2004.01.029.

[28] D. Jamet, C. Misbah, Toward a thermodynamically consistent picture of the phase-field model of vesicles: curvature energy, Phys. Rev. E 78 (2008) 031902, http://dx.doi.org/10.1103/PhysRevE.78.031902.

[29] G.-H. Cottet, E. Maitre, T. Milcent, Eulerian formulation and Level-Set models for incompressible fluid–structure interaction, Math. Model. Numer. Anal. 42 (2008) 471–492, http://dx.doi.org/10.1051/m2an:2008013.

[30] A. Laadhari, P. Saramito, C. Misbah, Vesicle tumbling inhibited by inertia, Phys. Fluids 24 (2012) 031901, http://dx.doi.org/10.1063/1.3690862.

[31] A. Laadhari, P. Saramito, C. Misbah, Computing the dynamics of biomembranes by combining conservative level set and adaptive finite element methods, J. Comput. Phys. 263 (2014) 328–352, http://dx.doi.org/10.1016/j.jcp.2013.12.032.

[32] V. Doyeux, Y. Guyot, V. Chabannes, C. Prud'homme, M. Ismail, Simulation of two-fluid flows using a finite element/level set method. Application to bubbles and vesicle dynamics, J. Comput. Appl. Math. 246 (2013) 251–259, http://dx.doi.org/10.1016/j.cam.2012.05.004, Fifth International Conference on Advanced Computational Methods in Engineering.

[33] M. Ismail, A. Lefebvre-Lepot, A necklace model for vesicles simulations in 2d, Int. J. Numer. Methods Fluids 76 (11) (2014) 835–854, http://dx.doi.org/10.1002/fld.396.

[34] C. Pozrikidis, Numerical simulation of the flow-induced deformation of red blood cells, Ann. Biomed. Eng. 31 (2003) 1194–1205, http://dx.doi.org/10.1114/1.1617985.

[35] A. Rahimian, S.K. Veerapaneni, G. Biros, Dynamic simulation of locally inextensible vesicles suspended in an arbitrary two-dimensional domain, a boundary integral method, J. Comput. Phys. 229 (18) (2010) 6466–6484, http://dx.doi.org/10.1016/j.jcp.2010.05.006.

[36] Y. Kim, M.-C. Lai, Simulating the dynamics of inextensible vesicles by the penalty immersed boundary method, J. Comput. Phys. 229 (12) (2010) 4840–4853, http://dx.doi.org/10.1016/j.jcp.2010.03.020.

[37] W.-F. Hu, K.Y. Kim, M.-C. Lai, An immersed boundary method for simulating the dynamics of three-dimensional axisymmetric vesicles in Navier–Stokes flows, J. Comput. Phys. 257 (Part A) (2014) 670–686, http://dx.doi.org/10.1016/j.jcp.2010.03.020.

[38] W.R. Dodson, P. Dimitrakopoulos, Oscillatory tank-treading motion of erythrocytes in shear flows, Phys. Rev. E 84 (2011) 011913, http://dx.doi.org/10.1103/PhysRevE.84.011913.

[39] A. Bonito, R. Nochetto, M. Pauletti, Dynamics of biomembranes: effect of the bulk fluid, Math. Model. Nat. Phenom. 6 (2011) 25–43, http://dx.doi.org/10.1051/mmnp/20116502.

[40] J.W. Barrett, H. Garcke, R. Nürnberg, Finite element approximation for the dynamics of asymmetric fluidic biomembranes, Math. Comp. 86 (2017) 1037–1069, http://dx.doi.org/10.1090/mcom/3162.

[41] B. Kaoui, J. Harting, C. Misbah, Two-dimensional vesicle dynamics under shear flow: effect of confinement, Phys. Rev. E 83 (2011) 066319, http://dx.doi.org/10.1103/PhysRevE.83.066319.

[42] S. Hysing, A new implicit surface tension implementation for interfacial flows, Int. J. Numer. Methods Fluids 51 (6) (2006) 659–672, http://dx.doi.org/10.1002/fld.1147.

[43] M. Raessi, M. Bussmann, J. Mostaghimi, A semi-implicit finite volume implementation of the CSF method for treating surface tension in interfacial flows, Int. J. Numer. Methods Fluids 59 (10) (2009) 1093–1110, http://dx.doi.org/10.1002/fld.1857.

[44] A. Laadhari, G. Székely, Fully implicit finite element method for the modeling of free surface flows with surface tension effect, Int. J. Numer. Meth. Engng. (2016), http://dx.doi.org/10.1002/nme.5493, in press.

[45] J.M. Ortega, W.C. Rheinboldt, Iterative Solution of Nonlinear Equations in Several Variables, SIAM, Philadelphia, PA, USA, 1970.

[46] R.L. Bryant, A duality theorem for Willmore surfaces, J. Differ. Geom. 20 (1) (1984) 23–53, http://projecteuclid.org/euclid.jdg/1214438991.

[47] T. Willmore, Riemannian Geometry, Oxford University Press, USA, ISBN 0198514921, 1993.

[48] S. Osher, J.A. Sethian, Front propagating with curvature dependent speed: algorithms based on Hamilton–Jacobi formulations, J. Comput. Phys. 79 (12), http://dx.doi.org/10.1016/0021-9991(88)90002-2.

[49] M. Sussman, E. Fatemi, An efficient, interface preserving Level Set re-distancing algorithm and its application to interfacial incompressible fluid flow, SIAM J. Sci. Comput. 20 (4) (1998) 1165–1191, http://dx.doi.org/10.1137/S1064827596298245.

[50] M. Sussman, A.S. Almgren, J.B. Bell, P. Colella, L.H. Howell, M.L. Welcome, An adaptive level set approach for incompressible two-phase flows, J. Comput. Phys. 148 (1) (1999) 81–124, http://dx.doi.org/10.1006/jcph.1998.6106.

[51] P. Gomez, J. Hernandez, J. Lopez, On the reinitialization procedure in a narrow-band locally refined level set method for interfacial flows, Int. J. Numer. Meth. Engng. 63 (10) (2005) 1478–1512, http://dx.doi.org/10.1002/nme.1324.

[52] M. Herrmann, A balanced force refined level set grid method for two-phase flows on unstructured flow solver grids, J. Comput. Phys. 227 (4) (2008) 2674–2706, http://dx.doi.org/10.1016/j.jcp.2007.11.002.

[53] G.-S. Jiang, D. Peng, Weighted ENO schemes for Hamilton–Jacobi equations, SIAM J. Sci. Comput. 21 (6) (2000) 2126–2143, http://dx.doi.org/10.1137/S106482759732455X.

[54] D. Hartmann, M. Meinke, W. Schröder, Differential equation based constrained reinitialization for level set methods, J. Comput. Phys. 227 (14) (2008) 6821–6845, http://dx.doi.org/10.1016/j.jcp.2008.03.040.

[55] D. Hartmann, M. Meinke, W. Schröder, The constrained reinitialization equation for level set methods, J. Comput. Phys. 229 (5) (2010) 1514–1535, http://dx.doi.org/10.1016/j.jcp.2008.03.040.

[56] A. Laadhari, P. Saramito, C. Misbah, Improving the mass conservation of the level set method in a finite element context, C. R. Math. 348 (9) (2010) 535–540, http://dx.doi.org/10.1016/j.crma.2010.03.011.

[57] P. Saramito, Efficient C++ finite element computing with Rheolef, CNRS-CCSD ed., http://www-ljk.imag.fr/membres/Pierre.Saramito/rheolef/rheolef-refman.pdf, 2013, Accessed: 2017 April 18.

[58] Y. Evans, J. Spruck, Motion of level sets by mean curvature III, J. Geom. Anal. 2 (2) (1992) 121–150, http://dx.doi.org/10.1007/BF02921385.

[59] E. Hairer, G. Wanner, Solving Ordinary Differential Equations II, Stiff and Differential-Algebraic Problems, Springer Series in Computational Mathematics, vol. 14, Springer, Berlin, Heidelberg, ISBN 9783642052217, 1996.

[60] F. Brezzi, M. Fortin, Mixed and Hybrid Finite Element Methods, vol. 15, Springer, New York, 1991.

[61] A. Laadhari, G. Székely, Eulerian finite element method for the numerical modeling of fluid dynamics of natural and pathological aortic valves, J. Comput. Appl. Math., http://dx.doi.org/10.1016/j.cam.2016.11.042.

[62] P. Saramito, Complex Fluid Modelling and Algorithms, 1st edition, Springer International Publishing AG, ISBN 9783319443614, 2016.

[63] S. Hysing, S. Turek, D. Kuzmin, N. Parolini, E. Burman, S. Ganesan, L. Tobiska, Quantitative benchmark computations of two-dimensional bubble dynamics, Int. J. Numer. Methods Fluids 60 (11) (2009) 1259–1288, http://dx.doi.org/10.1002/fld.1934.

[64] L. Štrubelj, I. Tiselj, B. Mavko, Simulations of free surface flows with implementation of surface tension and interface sharpening in the two-fluid model, Int. J. Heat Fluid Flow 30 (4) (2009) 741–750, http://dx.doi.org/10.1016/j.ijheatfluidflow.2009.02.009.

[65] J. Klostermann, K. Schaake, R. Schwarze, Numerical simulation of a single rising bubble by VOF with surface compression, Int. J. Numer. Methods Fluids 71 (8) (2013) 960–982, http://dx.doi.org/10.1002/fld.3692.

[66] V. Kantsler, V. Steinberg, Orientation and dynamics of a vesicle in tank-treading motion in shear, Phys. Rev. Lett. 95 (2005) 258101, http://dx.doi.org/10.1103/PhysRevLett.95.258101.

[67] J. Beaucourt, F. Rioual, T. Séon, T. Biben, C. Misbah, Steady to unsteady dynamics of a vesicle in a flow, Phys. Rev. E 69 (2004) 011906, http://dx.doi.org/10.1103/PhysRevE.69.011906.

[68] H. Zhao, E.S.G. Shaqfeh, The dynamics of a vesicle in simple shear flow, J. Fluid Mech. 674 (2011) 578–604, http://dx.doi.org/10.1017/S0022112011000115.

[69] M. Kraus, W. Wintz, U. Seifert, R. Lipowsky, Fluid vesicles in shear flow, Phys. Rev. Lett. 77 (1996) 3685, http://dx.doi.org/10.1103/PhysRevE.72.011901.

[70] H. Noguchi, G. Gompper, Swinging and tumbling of fluid vesicles in shear flow, Phys. Rev. Lett. 98 (2007) 128103, http://dx.doi.org/10.1103/PhysRevLett.98.128103.